Modification of the Electrochemical Surface Oxide Formation and the Hydrogen Oxidation Activity of Ruthenium by Strong Metal Support Interactions

Björn M. Stühmeier,[1,=,*,z] Robin J. Schuster,[1,=] Louis Hartmann,[1,*] Sören Selve,[2] Hany A. El-Sayed,[1,a] and Hubert A. Gasteiger[1,**]

[1]Chair of Technical Electrochemistry, Department of Chemistry and Catalysis Research Center, Technical University of Munich, 85748 Garching, Germany
[2]Center for Electron Microscopy (ZELMI), Technical University of Berlin, 10623 Berlin, Germany

A major hurdle for the wide spread commercialization of proton exchange membrane based fuel cells (PEMFCs) and water electrolyzers are the durability and high cost of noble metal catalysts. Here, alternative support materials might offer advantages, as they can alter the properties of a catalyst by means of a strong metal support interaction (SMSI) that has been shown to prevent platinum oxidation and suppress the oxygen reduction reaction on titanium oxide supported platinum nanoparticles deposited on a carbon support (Pt/TiO$_x$/C). Herein, we report a novel Ru/TiO$_x$/C catalyst that according to tomographic transmission electron microscopy analysis consists of partially encapsulated Ru particles in a Ru/TiO$_x$-composite matrix supported on a carbon support. It is shown by cyclic voltammetry and X-ray photoelectron spectroscopy that ruthenium oxidation is mitigated by an SMSI between Ru and TiO$_x$ after reductive heat-treatment (Ru/TiO$_x$/C$^{400°C,H_2}$). As a result, the catalyst is capable of oxidizing hydrogen up to the onset of oxygen evolution reaction, in stark contrast to a Ru/C reference catalyst. PEMFC-based hydrogen pump measurements confirmed the stabilization of the hydrogen oxidation reaction (HOR) activity on Ru/TiO$_x$/C$^{400°C,H_2}$ and showed a ≈3-fold higher HOR activity compared to Ru/C, albeit roughly two orders of magnitude less active than Pt/C.

Water electrolyzers and hydrogen powered fuel cells are expected to play a key role in energy storage and production when transitioning to a carbon neutral economy based on renewable energy to combat climate change.[1,2] For both technologies, a major hurdle for wide-spread commercialization are the high system costs, whereby a significant fraction results from the use of noble metal based electrocatalysts. Proton exchange membrane fuel cells (PEMFCs) rely on Pt-based catalysts for the hydrogen oxidation reaction (HOR) and the oxygen reduction reaction (ORR).[3] Similarly, Pt-based hydrogen evolution reaction (HER) and Ir-based oxygen evolution reaction (OER) catalysts are used in proton exchange membrane water electrolyzers (PEMWEs).[4] Due to the sluggish kinetics of the ORR and OER, the main focus of catalyst development for these devices has been on reducing the noble metal loading of the respective oxygen electrodes by seeking to develop Pt-free ORR catalysts as well as highly active and durable Pt-alloy catalysts for low-loaded PEMFC cathodes,[5,6] and to reduce the anode loading of PEMWE systems.[7] On the contrary, the hydrogen side is often neglected with regards to potential catalyst cost savings. This is due to the extremely fast kinetics of the HER/HOR (Eq. 1) that allows for the use of metal loadings of ≈ 0.025–0.05 mg$_{Pt}$ cm$_{geo}^{-2}$,[8–10] which should be sufficient to reach target loadings of ≈0.125 mg$_{Pt}$ cm$_{geo}^{-2}$ for the whole membrane electrode assembly (MEA) of PEMFC systems.[11,12]

$$H_2 \rightleftharpoons 2\,H^+ + 2\,e^- \quad [1]$$
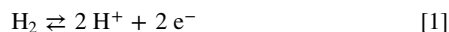
At such low Pt loadings, however, even a modest loss of electrochemically active surface area (ECSA) of either of the electrodes due to cell-reversal (CR) or start-up and shut-down (SUSD) events can lead to a noticeable performance degradation of the PEMFC.[6,13–16]

In this respect, Ru might offer advantages as an anode catalyst as it might mitigate some of the most detrimental ECSA degradation phenomena in PEMFCs: Ru in the form of ruthenium oxide is well known to be a highly active oxygen evolution catalyst,[17,18] and employing an OER catalyst on the anode has been shown to significantly increase the system durability in CR events.[19] Additionally, Ru is essentially inactive for the ORR,[20] which could significantly reduce cathode degradation during SUSD events, as was shown for iridium catalysts that have a high HOR activity and a low ORR activity.[21] Finally, it exhibits a high CO tolerance, which might reduce the required purification efforts to remove CO from reformate gas.[22] However, the HOR on ruthenium catalysts is inhibited by hydroxide adsorption even at low overpotentials,[23,24] preventing its use as a commercial anode catalyst. In order to enable the use of ruthenium as an alternative to platinum based HOR catalyst, the (surface-)oxidation of metallic ruthenium would have to be suppressed and the thus stabilized catalyst would need to have at least 10% of the mass activity of Pt (i$_0$ = 540 ± 160 A mg$_{Pt}^{-1}$)[25] and a similar long term stability in order to be of any practical advantage.

In recent years, the field of oxide supported metal nanoparticles has gained interest due to the unique properties of a strong metal-support interaction (SMSI) effect that can dramatically alter the catalytic properties of the metal. The SMSI is characterized by a modified bonding interaction between the metal and a partially reduced oxide support that in most cases results in an encapsulation of the metal nanoparticles by a thin (sub-)oxide layer.[26–29] The driving force for this encapsulation is widely considered to be the minimization of the surface energy of the nanoparticles.[30,31] When it comes to the alteration of the electrocatalytic behavior of such systems, it was shown that when a Nb-doped TiO$_2$ supported Pt catalyst was exposed to voltage cycling between 1.0–1.4 V vs the reversible hydrogen electrode (RHE), Pt oxidation features and ORR activity were apparently reduced without affecting the HOR activity; this was explained by selective Pt-site blocking through the dissolution and re-deposition of a very thin layer of the oxide support (on the order of one to a few monolayers) on the Pt surface.[32] Depending on the thickness, such thin oxide layers might significantly affect the charge transport mechanism and therefore

=Equal Contribution.
*Electrochemical Society Student Member.
**Electrochemical Society Fellow.
aCurrent Address: Freudenberg Fuel Cell e-Power Systems GmbH, Bayerwaldstr. 3, 81737 München, Germany.
zE-mail: bjoern.stuehmeier@tum.de

alter the electrochemical reactivity of the catalyst.[33] Similarly, a TiO$_2$ supported Pt catalyst that was exposed to reductive conditions during the atomic layer deposition of Pt or in H$_2$ atmosphere showed an HOR activity of Pt that was stabilized up to 1.5 V$_{RHE}$, while the ORR activity was almost completely suppressed.[34,35] While some of these effects have been explained by a change in conductivity of the oxide support material depending on the atmosphere,[36] other studies suggest that a proton conducting monolayer-thick film of (sub-)oxide encapsulates the nanoparticles and prevents oxygenated species from reaching the metal surface, thereby stabilizing the reduced state of the metal nanoparticles.[32,34,35,37,38] It seems reasonable to speculate that the HOR activity of other HER/HOR active metals such as Ru might be preserved in a similar fashion at potentials where a deactivation due to surface oxidation would occur otherwise. Indeed, it was recently shown by Zhou et al. that Ru clusters can be stabilized against oxidation in a TiO$_2$ matrix while remaining active for the HOR beyond 0.5 V$_{RHE}$ even when poisoned by CO.[39]

In this study, we present a novel Ru/TiO$_x$/C ($x \leqslant 2$) catalyst that is capable of oxidizing hydrogen up to the onset of the OER at 1.3 V$_{RHE}$. This catalyst is based on the deposition of Ru nanoparticles on nano-sized titanium oxide particles, the subsequent adsorption of the resulting Ru/TiO$_x$ particles onto high-surface area carbon Vulcan carbon (Ru/TiO$_x$/C), and a reductive treatment in H$_2$-containing atmosphere at 400 °C (Ru/TiO$_x$/C$^{400°C,H_2}$). After a detailed structural investigation of the hierarchical catalyst by transmission electron microscopy (TEM) using a tomographic tilt-series in combination with selective area electron diffraction (SAED), the stability against oxidation of the catalyst is compared to a Ru/C reference catalyst by means of rotating disk electrode (RDE) measurements and ex-situ X-ray photoelectron spectroscopy (XPS). Based on the differences in oxidation behavior, the retention of the HOR activity and the effect of the SMSI on the OER activity, as observed in RDE, is discussed. Finally, catalysts were implemented in membrane electrode assemblies (MEAs) in order to quantify their HOR/HER activity via PEMFC-based hydrogen pump measurements. The implications on the usability of Ru-based catalysts for the hydrogen side of PEMFC will be discussed.

Experimental

Catalyst synthesis.—The Ru/TiO$_x$/C catalysts were prepared based on a previously reported multistep synthesis procedure for Pt/TiO$_x$/C catalysts,[35] whereby the key synthesis steps and adaptations are described in the following. First, Ru-nanoparticles (Ru-NP) were prepared using the polyol reduction method: 150 mg RuCl$_3$ (45%–55% Ru content, Sigma Aldrich) and 75 mg polyvinylpyrrolidone (PVP, average Mw ≈55000, Sigma Aldrich) were dissolved in 500 ml of water-free ethylene glycol (EG, 99.8%, anhydrous, Sigma Aldrich), deaereated by argon (6.0-grade, Westfalen AG), then the solution was heated from room temperature to 155 °C at a constant rate of 4 °C min^{-1} (controlled by a temperature controller; model 310, J-KEM), kept there for 90 min, and subsequently was allowed to cool down to room temperature. Meanwhile, a solution of 0.84 ml titanium(IV)isopropoxide (≥97%, Sigma Aldrich Corp.) in 75 ml ethanol (EtOH, 99.8%, absolute, Sigma Aldrich Corp.) was added dropwise over the course of ca. 10 min to 75 ml of high purity water (H$_2$O, 15 MΩ·cm, E-POD, Merck Millipore KGaA) held at 80 °C. After stirring for 60 min, 150 ml EG were added and the titania dispersion was allowed to cool down to room temperature.

Then, H$_2$O and EtOH were evaporated using a rotary evaporator (Hei-VAP Value; Heidolph Instruments GmbH & CO. KG.) resulting in a titania dispersion in the remaining EG. Subsequently, the Ru-NP suspension was added to the titania dispersion and stirred for 24 h at room temperature. The suspension of the resulting Ru/TiO$_x$-composite ($x \leqslant 2$, whereby TiO$_x$ might be partially hydrated)[35] was added to a suspension of 108 mg Vulcan carbon (XC-72R, Tanaka Kikinzoku International K. K., Japan) dispersed by ultrasonication in 150 ml EG and stirred for another 48 h. Afterwards, the volume of the suspension was doubled with acetone (≥98%, Sigma Aldrich Corp.), stirred for another 12 h, and centrifuged at 11000 rpm at 10 °C in an ultra-centrifuge (5810 R, Eppendorf) to separate the Ru/TiO$_x$/C catalyst and the solvent. Finally, the catalyst was washed three times with a 50/50 (v/v) acetone/water mixture and dried at 70 °C in air to obtain the Ru/TiO$_x$/C$^{as-synth.}$ catalyst. Finally, a heat treatment at 400 °C (10 K min^{-1}) for 1 h under reductive atmosphere (5% H$_2$/Ar) was performed to obtain the Ru/TiO$_x$/C$^{400°C,H_2}$ catalyst.

The elemental composition of Ru/C and Ru/TiO$_x$/C$^{400°C,H_2}$ was determined by inductively coupled plasma mass spectrometry (ICP-MS) after acid digestion (aqua regia according to the procedure proposed by Suoranta et al.[40] for Ru and sulfuric acid for Ti), and by carbon oxidation at elevated temperatures in air. The results are given in Table I. Note that the samples were analyzed as stored under ambient conditions. Thus, the total masses add up to less than 100% when considering only Ru, TiO$_2$, and C due to water adsorption and, in the case of Ru/C, ruthenium bulk oxidation.

Transmission electron microscopy and electron diffraction.— The powders of each specimen were dispersed in pure ethanol and sonicated for 5 min 3 μl of the dispersion was drop-casted on 300 mesh lacey-carbon cupper grids and air-dried at 40 °C. TEM, high resolution (HR-)TEM, and electron diffraction investigations were performed at an FEI TECNAI G^{2}20 S-Twin transmission electron microscope with LaB6 emitter, operated at 200 kV. TEM images were acquired with a Gatan 1kx1k MSP794 P CCD-camera. The microscope is further equipped with an EDAX r-TEM SUTW EDX detector, a customized DISS6 scan unit by point electronic GmbH, and a combined BF-ADF-HAADF-STEM detector from PN-Detector for STEM investigations and qualitative elemental mappings.

Tomographic tilt-series were acquired in TEM-mode for alpha-tilts between −60° and +70° using a Fischione Dual-Axis Tomography Holder Model 2040. For tomographic data processing, the IMOD and etomo software were used; DigitalMicrograph was used for evaluating HR-/TEM images and diffraction patterns; the EDAX Genesis Software was used for EDX-data acquisition and evaluation.

Rotating disk electrode, hardware and preparation.—The electrode and ink preparation, as well as the setup and measurement procedure were already reported in previous publications by our group.[41–43] For the preparation of the electrolytes and for the rinsing of the measurement components, 18.2 MΩ cm deionized water (Milli-Q Integral 5, Merck Millipore KGaA) was used. Glassy Carbon (GC) electrodes (5 mm diameter, Pine Research Instrumentation) fixed in a PTFE-body (Pine Research Instrumentation) were used as working electrodes (WE). The GC substrates were polished with a 0.05 μm Al$_2$O$_3$ polishing suspension (Bühler AG) and sonicated various times in

Table I. Weight percentages of Ru, Ti, and C in the catalyst samples as obtained by ICP-MS and carbon oxidation. The remaing mass percentages up to 100% are due to the oxygen in the titanium oxide, the largely oxidized form of ruthenium NPs, and adsorbed water.

Catalyst	Ru-Content [wt.%]	Ti-Content [wt.%]	C-Content [wt.%]
Ru/C	17.1	—	67.6
Ru/TiO$_x$/C$^{400°C,H_2}$	8.8	28.6	23.3

Milli-Q water. Inks were prepared by adding high purity acetone (⩾99.9%, Chromasolv Plus, for HPLC, Sigma Aldrich Corp.) to the dry catalyst. The catalyst content in the ink was adjusted to achieve Ru loadings of ≈20 μg_{Ru} cm_{disk}^{-2} (corresponding to ≈0.09 mg_{Vulcan} cm_{disk}^{-2}, which yields a catalyst layer film thickness of ≈3 μm (based on a packing density of ≈28 μm (mg_{Vulcan} $cm_{disk}^{-2})^{-1}$ on the glassy carbon disk).[44] The catalyst suspension was sonicated in a sonication bath (Elmasonic S 30 H, Elma Schmidbauer GmbH), maintaining the bath temperature at less than 25 °C to avoid evaporation of the solvent. Nafion (5 wt.% in lower aliphatic alcohols, 15%–20% H_2O, Sigma Aldrich Corp.) was then added to the suspension, resulting in an ionomer to support (C + TiO_x) ratio of 0.1 g_I g_S^{-1}, followed by sonication in a weaker sonication bath (USC100T, VWR International GmbH) for at least 10 min 10 μl of ink were dropped on a GC disk, which was subsequently covered with a small glass vial. As still some catalyst (≈5%–10%) remained as an unsuspended sediment, 10 μl of ink were dropped in parallel on each of six aluminum foil pieces (10 mm diameter), whose blank weight prior to applying the ink had been determined with an ultra-high precision balance (XP6, Mettler-Toledo GmbH). After drying at room temperature, the actual catalyst loading on the disk was inferred to be 17 ± 2 μg_{Ru} cm_{disk}^{-2} based on the mass of the catalyst deposits on the aluminum foil samples.

Electrolyte solutions were prepared from high purity $HClO_4$ (60%, Guaranteed Reagent, Kanto Chemical Co., Inc., Japan) by addition of ultrapure water. Argon and hydrogen gases used for purging the electrolyte were of high purity (6.0-grade, Westfalen AG). A glass cell with a Pt mesh as the counter electrode that was separated by a glass frit from the working electrode compartment was used. As reference electrode (RE), a static hydrogen RE was used as a reversible hydrogen electrode (RHE), consisting of a Pt wire (1.0 mm diameter; >99.99% purity, ADVENT Research Materials Ltd., UK) sealed into a glass tube that was partially filled with the same electrolyte as that used for the RDE measurements and whose other end was drawn to a capillary; a hydrogen bubble was evolved electrolytically inside the glass tube prior to usage.[45] The capillary was immersed into the electrolyte and, separated from the RDE compartment with an electrolyte bridge. This reference electrode (RE) was freshly prepared each day and calibrated against a polycrystalline Pt disk electrode in H_2 saturated electrolyte and. Electrochemical measurements were performed using an Autolab potentiostat (PGSTAT302N, Metrohm AG, Switzerland) equipped with an analog potential scan module, a frequency response analyzer, and a bipotentiostat module. A rotator with a polyether ether ketone shaft (Pine Research Instrumentation, USA) was used.

Rotating disk electrode measurements.—Prior to any measurements, the catalysts were cleaned by cycling the potential 25 times between 0.0 and 1.0 V_{RHE} at 100 mV s^{-1} in an Ar-saturated electrolyte, after which steady-state CVs were obtained, directly followed by CV measurements (3 cycles each) at 20 mV s^{-1} with a lower potential limit of 0.02 V_{RHE} and an upper potential limit increasing in 0.1 V steps from 0.6 to 1.3 V_{RHE}. The high frequency resistance (HFR in Ω) between WE and RE was determined by electrochemical impedance spectroscopy (EIS) from 100 kHz to 100 Hz at the open circuit voltage (OCV) with an amplitude of 10 mV. Potentials corrected according to Eq. 2 are denominated $E_{iR-free}$, whereby E is the potential and I the current (note that cathodic currents are taken to be negative):

$$E_{iR-free} = E - I \cdot HFR \qquad [2]$$

The geometric current density i_{geo} (Eq. 3) is normalized by the area of the electrode (A_{disk} = 0.196 cm^2).

$$i_{geo} = I \cdot A_{electrode}^{-1} \qquad [3]$$

Prior to the HER/HOR measurements, the electrolyte was saturated with H_2. While recording the HER/HOR polarization curves, the H_2 flow was set to blanketing the cell head space. The potential was cycled between −0.05 and 1.3 V_{RHE} at rotation rates going from 2500 to 200 rpm, followed by a single HER/HOR curve up to 1.5 V_{RHE} at 1600 rpm.

X-ray photoelectron spectroscopy measurements.—Nafion-free dispersions of Ru/C and Ru/TiO$_x$/C$^{400°C,H_2}$ were prepared as described for the TEM measurements and the catalysts were drop-casted in close proximity of each other on gold foils (0.025 mm thickness, 99.99% purity, ADVENT Research Materials Ltd., UK). Subsequently, the samples containing the catalysts were submerged in Ar-saturated 0.1 M $HClO_4$ and polarized to 0.02 V_{RHE} for 600 s, followed by an oxidation at either 0.8, 1.0, or 1.3 V_{RHE} for another 600 s. The samples were then dipped three times in an excess of Milli-Q water and dried in vacuo at 70 °C overnight.

The surface analysis of these samples was carried out by X-ray photoelectron spectroscopy (Axis, Supra, Kratos, UK). A PEEK-sample holder in a floating ground configuration was used to avoid differential charging. The samples were kept in the antechamber until a pressure of ≈10^{-8} Torr and were then transferred to the sample analysis chamber (SAC) where the pressure was always kept at ≈10^{-9} Torr during the whole measurement period. Sample irradiation was carried out with monochromatic Al Kα radiation (1486.6 eV) with an emission current of 15 mA. For the Ag 3d$_{5/2}$ line, the full width at half-maximum (FWHM) was 1.02 eV under the recording conditions (using a pass energy of 0.05 eV). Elemental spectra were recorded with a step size of 0.05 eV and an emission current of 15 mA and a pass energy of 0.05 eV. Low energy electrons were used for charge neutralization and the spectra were calibrated to the elemental Au 4f$_{7/2}$ peak from the substrate with a binding energy (BE) of 83.95 eV. To avoid any errors in charge neutralization, the binding energy differences of the different elemental peaks in the survey spectra were compared. Short acquisition time spectra in the O 1s region were recorded before and after each set of experiments in order to check that the samples did not suffer from radiation damage.

The XPS data analysis was performed using the Casa XPS software. A Shirley function was used as background. As it is reported that Ru 3d spectra exhibit a distinct asymmetric line shape, a Functional Lorentzian line shape was used for metallic ruthenium and for ruthenium oxides, with the parameters set to A(0.5,1,0)GL(0).[46] The fits of the doublets of Ru 3d$_{5/2}$ and Ru 3d$_{3/2}$ were fixed to have the same FWHM and to have a (3d$_{5/2}$)/(3d$_{3/2}$) peak area ratio of 3:2 with a fixed separation of the peak maxima of 4.17 eV.[46] The C 1s peaks were fitted using a mixture of a Lorentzian (30%) and Gaussian (70%) shape function[47]; the constraints on binding energy and full width at half maximum (FWHM) for the different species are given in Table. II. For the ease of the reader only the Ru-fits are shown below. In-house reference spectra of TiO_2, carbon, metallic Ru and anhydrous RuO_2 were used to determine the binding energy and FWHM.

Table II. XPS peak fitting parameters used for identification and quantification of the different surface species of the measured samples.

Element/ Region	Assigned Species	Binding Energy [eV] (constrained range)	FWHM [eV] (constrained range)
Ruthenium Ru 3d	Ru^0	280.1 (±0.1)	0.7–1.0
	Ru^{4+}	281.3 (±0.1)	0.7–1.0
Carbon C 1s	C–C sp^2	284.8 (±0.1)	1.0–1.3
	C–C sp^3	284.4 (±0.1)	1.0–1.3
	C–O	289.8 (±0.1)	1.5–2.25
Gold Au 4f	Au^0	83.95 (fixed)	1.5–2.25

Fuel cell hardware & MEA preparation.—All hydrogen-pump measurements were performed on a customized G60 test station (Greenlight Innovation Corp., USA) modified to feature pure H_2 instead of air/O_2 on the cathode side; there were also no CO gas connections in order to avoid any unintentional poisoning with CO. The current range of the potentiostat (Reference3000, Gamry Instruments, USA) was extended by a booster (Reference 30K Booster, Gamry Instruments, USA). All measurements were carried out with an in-house designed 5 cm^2 active area single-cell hardware, using commercial graphite flow fields (7 parallel channels, one serpentine, 0.5 mm lands/channels; manufactured by Poco Graphite, Entegris GmbH, Germany, according to our design).[48] Gas diffusion layers (GDLs) were the same in all experiments (H14C10, Freudenberg KG, Germany) and the GDL compression was adjusted to 13 ± 1% by quasi-incompressible, PTFE-coated fiberglass gaskets (Fiberflon, Fiberflon GmbH & Co. KG, Germany), assembled at a torque of 12 Nm, resulting in a contact pressure of ≈1.5 MPa on the active area (for details see Simon et al.).[49]

MEAs were prepared by the decal transfer method. The catalyst inks were prepared by ball milling (200 rpm, 3 min on, 5 min off, 5 cycles) a defined amount of catalyst (Ru/C or Ru/TiO$_x$/C$^{400°C,H_2}$) with 1-propanol in a 20 ml jar containing 16 g of ZrO$_2$ beads (2 mm diameter) with a solid content of 0.03 g mL$_{ink}$$^{-1}$. Afterwards, the catalyst dispersion was transferred into a smaller bottle, to which an ionomer solution (low equivalent weight, Asahi Kasai Corp.) corresponding to an I/S ratio of 0.65/1 g$_I$ g$_S$$^{-1}$ (based on the weight of the transferred ink) was added, and the ink mixing was completed by placing the bottles onto a roller-mill at 100 rpm for 18 h at 25 °C. For the CE, a Pt/C catalyst (45.6wt.% Pt, TEC10V50E, Tanaka) was directly mixed with 1-propanol and ionomer solution on the roller mill (water concentration: 16wt.%; solid content: 0.04 g mL$_{ink}$$^{-1}$; I/C: 0.65/1 g$_I$ g$_C$$^{-1}$). Then, the Mayer rod technique (K Control Coater, RK PrintlCoat Instruments Ltd., England) with the appropriate bar size was used to achieve loadings of ≈ 50 μg$_{Ru}$ cm^{-2}$_{MEA}$ (WE) and 0.39 ± 0.02 mg$_{Pt}$ cm^{-2}$_{MEA}$ (CE) on virgin PTFE decals. The unsymmetrical MEAs were fabricated by hotpressing the air-dried decals onto a 15 μm membrane (W. L. Gore & Associates GmbH) at 155 °C for 3 min with an applied pressure of 0.11 kN cm^{-2}.

H$_2$-pump measurement procedure.—The measurement procedure was already reported in a previous publication by our group.[25] Prior to any kinetic measurements, each cell was conditioned to activate the catalyst using a voltage-controlled ramp-in procedure in a H$_2$/H$_2$ setup (80 °C, 90% relative humidity (RH), flow rates of 2000/2000 nccm at a H$_2$ partial pressure of 450/450 kPa$_{H_2}$): −0.35 V for 15 min, 5 min at open circuit voltage (OCV), and 0.35 V for 10 min This sequence was repeated four times until a constant performance was reached. The kinetic measurements were then performed at 80 °C and 100 kPa$_{H_2}$ in H$_2$/H$_2$ (2000/2000 nccm) configuration at 90% RH. Cyclic voltammograms (CVs) were recorded between −0.3 V and +0.6 V at scan rates of 100 mV s^{-1} (20 cycles) and then at 5 mV s^{-1} (3 cycles), followed by a galvanostatic electrochemical impedance spectroscopy (EIS) at OCV with a 2 mA cm$_{MEA}$$^{-2}$ AC current perturbation between 500 kHz and 1 Hz (10 points per decade) to determine the HFR (in mΩ cm$_{MEA}$^{2}) that was used for correcting the cell potential E$_{cell}$ for the Ohmic drop, yielding the iR-free cell voltage (E$_{iR-free}$) according to Eq. 2. These potentiodynamic measurements were followed by a set of galvanostatic and potentiostatic measurements. For galvanostatic measurements, a DC current was drawn for 60 s and the resulting potential response was averaged over the last 10 s; this was followed by an EIS measurement at the same current, with a current amplitude of 10% of the DC current (from 500 kHz to 1 Hz, with 10 points per decade). These measurements were performed for four currents between ±0.0117 A cm$_{MEA}$$^{-2}$ and ±0.074 A cm$_{MEA}$$^{-2}$ in ascending order by alternating between anodic and the corresponding cathodic current in order to precisely determine the reversible potential at each condition.

Following these galvanostatic measurements, potentiostatic measurements were conducted in the analogous manner by applying a given potential for 60 s and averaging the resulting current during the last 10 s, followed by a potentiostatic EIS at the same potential using a potential amplitude of 1% of the DC potential (from 500 kHz to 1 Hz, with 10 points per decade).The potentiostatic testing was performed for potentials between ±5 mV and in the range between −200 mV and + 450 mV; this was done in ascending order and by alternating between anodic and equal cathodic potentials. Each data point was corrected for the HFR at this specific potential. Considering that the WE was very thin (ca. 6 μm) and that the HOR/HER overpotential of the high-loaded Pt based CE is negligible, the HFR-corrected cell voltage very closely represents the HOR/HER overpotential η:

$$\eta = E_{iR-free}(E) = E_{cell} - i \times HFR(E_{cell}) \qquad [4]$$

After each data point (static hold plus EIS), a relaxation step of 5 or 30 s (after potentials exceeding ±0.1 V) at OCV was implemented to ensure steady-state conditions for the next point.

Finally, CVs of the WE were recorded between 0.05 and 1.0 V$_{RHE}$ at a scan rate of 100 mV s^{-1}, at 40 °C and ambient pressure. The CE was fed with 200 nccm of fully humidified 5% H$_2$ in Ar, and the WE was initially purged with dry N$_2$ at 50 nccm, while interrupting the gas flow to record the CVs.

Results and Discussion

Structural characterization by transmission electron microscopy.—To ensure that the catalyst synthesis steps would yield the desired structural characteristics, the morphology of the as-synthesized Ru/TiO$_x$/C$^{as-synth.}$ catalyst, consisting of Ru-NPs supported on larger TiO$_x$ nanoparticles which in turn are supported on Vulcan carbon, and of the subsequently reduced Ru/TiO$_x$/C$^{400°C,H_2}$ catalyst was analyzed by TEM (Fig. 1). For comparison, a carbon supported ruthenium catalyst prepared from the same Ru-NPs and the same Vulcan carbon support (Ru/C) served as reference catalyst and as a baseline for the characterization of the Ru/TiO$_x$/C catalysts, as it allows for a precise analysis of Ru-NP shape, size, and distribution. Furthermore, the non-heat-treated Ru/TiO$_x$/C$^{as-synth.}$ catalyst was examined to monitor the distribution of Ru-NPs throughout the catalyst, offering a way to confirm the targeted Ru-NP deposition onto the TiO$_x$ particles. At the end, the final Ru/TiO$_x$/C$^{400°C,H_2}$ catalyst was investigated for the effect of the reductive heat-treatment on the catalyst morphology.

The Ru-NPs were prepared by the polyol reduction method with PVP as a capping agent that resulted in spherical particles. The TEM image of the Ru/C reference catalyst (Fig. 1a) displays a homogeneous distribution of Ru-NPs and small agglomerates thereof on the surface of the Vulcan carbon support. Using higher magnified images (one representative example shown in Fig. 1e), the Ru particle diameter (d$_i$ in nm) was determined for at least 100 particles (Fig. 1h, green bars). The Sauter mean diameter (SMD) was calculated according to Eq. 5 as ≈2.2 nm for the Ru/C catalyst.

$$SMD = \frac{\sum d_i^3}{\sum d_i^2} \qquad [5]$$

This small particle size was desired to achieve a high electrochemically active surface area (ECSA), which in the spherical particle approximation would be inversely proportional to the SMD (i.e., ECSA = 6/(SMD · ρ_{Ru}), with ρ_{Ru} = 12.2 · 10^6 g m^{-3}).

The preparation route for the Ru/TiO$_x$/C$^{as-synth.}$ catalyst was designed to deposit the Ru-NPs on TiO$_x$ ("Ru/TiO$_x$-composite") to enable the later formation of an SMSI, which is not possible for Ru-NPs supported on carbon. The TEM images of the Ru/TiO$_x$/C$^{as-synth.}$ catalyst (Figs. 1b and 1f) indicate that the synthesis strategy to support Ru/TiO$_x$-composites on the carbon was largely successful. While the weak contrast of Ru↔TiO$_x$ and TiO$_x$↔C complicates the
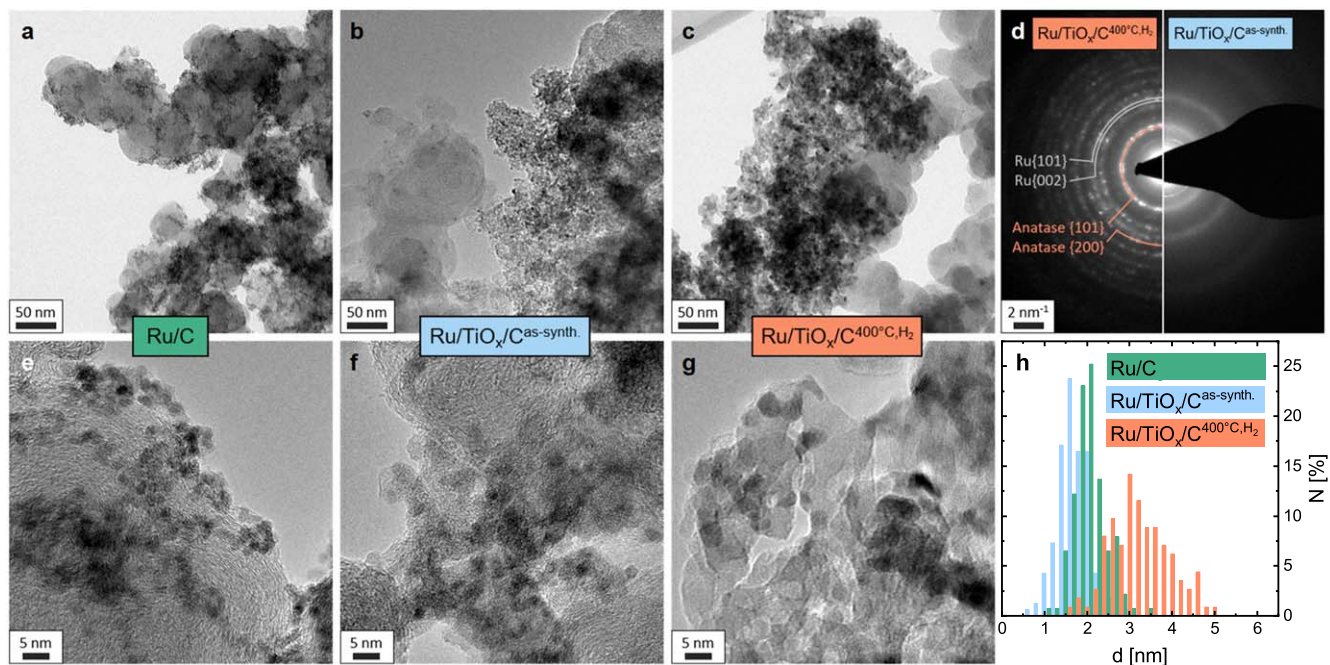
Figure 1. (HR) TEM images of the various prepared catalysts. (a) and (e) Ru/C, showing the distribution of Ru nanoparticles and small agglomerates on the carbon support; (b) and (f) Ru/TiO$_x$/C$^{as-synth.}$, with the Ru/TiO$_x$-composites attached to the carbon support, showing only few isolated Ru-NPs on the carbon; and, (c) and (g) Ru/TiO$_x$/C$^{400°C,H_2}$ consisting of agglomerates of larger Ru particles and crystalline TiO$_x$ that are supported on carbon. Panel (d) shows a comparison of the SAED patterns of Ru/TiO$_x$/C$^{400°C,H_2}$ (left half of the image) and of Ru/TiO$_x$/C$^{as-synth.}$ (right half), emphasizing the high crystallinity of Ru and anatase type TiO$_2$ after the heat-treatment. Pandel h) shows the Ru particle size distributions for the three catalysts, showing small particles on the as-synthesized samples (green and blue bars) and severe sintering after the heat-treatment at 400 °C (orange bars).

interpretation, the structural differences of the well-defined carbon spheres compared to the irregular shape of the Ru/TiO$_x$ agglomerates nevertheless allow to distinguish between Ru/TiO$_x$-composites and the mostly Ru-NP-free carbon although a few isolated Ru particles can be seen on the carbon support in Fig. 1b. A tomographic TEM tilt series was recorded to explore the large-scale three-dimensional (3D) catalyst structure (see the file RuTiOxC_TOMO.avi, with a scale bar of 100 nm, in the supporting information (available online at stacks.iop.org/JES/169/034519/mmedia)). Here, the differently sized and irregularly shaped Ru/TiO$_x$-composites are clearly deposited on and between the spherical primary particles of the carbon support and even some of the smaller particles on the carbon seem to be Ru/TiO$_x$-composites that did not aggregate to larger agglomerates based on the 3D structure. The determined particle size distribution (Fig. 1h, blue) has a similar shape as that of the Ru/C reference catalyst, with a calculated SMD of ≈2.0 nm. This minor decrease in average particle size can be explained by the fact that a fresh batch of Ru-NPs was prepared for each catalyst and small deviations were therefore expected. Additionally, the particle size determination for Ru-NPs on TiO$_x$ was further complicated by the poor contrast, which could potentially have resulted in a systematic underestimation of the particle size, as the particle edge was not well defined in all cases.

The Ru/TiO$_x$/C$^{as-synth.}$ catalyst was heat-treated at 400 °C under reductive atmosphere (5% H$_2$ in Ar, see experimental section) to obtain the final Ru/TiO$_x$/C$^{400°C,H_2}$ catalyst. The overall catalyst morphology consisting of Ru/TiO$_x$-composite agglomerates on the carbon support was maintained after the heat treatment (see Fig. 1c and the file RuTiOxC-400_TOMO.avi, with a scale bar of 200 nm, in the SI (available online at stacks.iop.org/JES/169/034519/mmedia)). This was confirmed by EDX mappings, where a Ru signal was always accompanied by a strong Ti signal proving the preferential deposition of Ru on the TiO$_x$ support (see Fig. A·1). However, the structure of the Ru/TiO$_x$-composites was significantly altered (Fig. 1g): While the TiO$_x$ had been mostly amorphous in the as-synthesized catalyst, the heat-treatment resulted in mostly

crystalline TiO$_2$ particles of the anatase-type (see indicated anatase-TiO$_2${101}, and anatase-TiO$_2${200} lattice planes), as seen in the selected area electron diffraction (SAED) patterns (Fig. 1d). For Ru/TiO$_x$/C$^{as-synth.}$ (right half of the image), the SAED only showed almost amorphous rings of low intensity, whereas for Ru/TiO$_x$/C$^{400°C,H_2}$ (left half), the intensity of the rings was much higher and additional Bragg-reflexes could be observed for both Ru (see indicated Ru{101} and Ru{002} lattice planes) and TiO$_2$. While the TiO$_2$ particles clearly increased in crystallinity as seen from the TEM images, the pronounced reflexes of Ru might at part be the result of a severe increase in particle size after the heat-treatment due to particle sintering as well. The low contrast of Ru↔TiO$_2$ in combination with a thickness contrast in TEM images complicated the identification of Ru-NPs. The Ru particle size (Fig. 1h, orange) was thus determined from a high-resolution tomographic TEM tilt series (see file HR_RuTiOxC-400_TOMO.avi, with a scale bar of 20 nm, in the SI (available online at stacks.iop.org/JES/169/034519/mmedia)) by identifying individual Ru particles from TEM images recorded at slightly different angles (see Fig. A·2 for examples). The resulting particle size distribution was much broader, with an SMD of 4.4 nm. Interestingly, some of the Ru particles seem to be incorporated into the TiO$_2$ structure rather than sitting on the surface. While it cannot be excluded that this might be the result of Ru sitting in cavities of the TiO$_2$ flakes/particles, it is likely the result of an encapsulation of the Ru-NPs by a thin TiO$_x$ (x ⩽ 2) layer that is well known to occur when an SMSI is formed.[27,29,50,51]

Electrochemical characterization in aqueous HClO$_4$ electrolyte.—To investigate whether an SMSI between Ru and TiO$_2$ in the Ru/TiO$_x$/C$^{400°C,H_2}$ catalyst might also prevent the surface oxidation of ruthenium and thereby stabilize the HOR activity at high potentials, analogous to what had been observed for a similarly prepared Pt/TiO$_x$/C$^{400°C,H_2}$ catalyst,[35] RDE measurements in 0.1 M HClO$_4$ were performed. Figure 2 shows the cyclic voltammograms (CVs) of the Ru/C (green line), the Ru/TiO$_x$/C$^{as-synth.}$ (blue line), and the Ru/TiO$_x$/C$^{400°C,H_2}$ (orange line) catalysts recorded in

Ar-saturated electrolyte. One difficulty in analyzing the voltammetric response of Ru-based catalysts is the distinction between hydrogen underpotential deposition (H_{upd}), double layer capacity, and surface oxidation that all overlap in the same potential regions.[52] It is known that the Ru-surface oxidation to RuO_2 is a complex multistep process via RuO and Ru_2O_3 that starts above 0.2 V_{RHE} in the anodic scan.[53] While an increasing extent of surface oxidation with increasing potential is clearly visible for the Ru/C reference catalyst, this process seems to be strongly suppressed for both Ru/TiO$_x$/C catalysts. Since the Ru to carbon ratio was similar in all catalysts, the capacitive contribution of the carbon support can be estimated by recording a CV of the corresponding amount of Vulcan-carbon on the GC (gray dashed line in Fig. 2). Thus, the much lower currents above 0.3 V_{RHE} for the Ru/TiO$_x$/C catalysts cannot result from the carbon support double layer capacity but must be related to the surface properties of the ruthenium. The high voltammetric currents of the Ru/C catalyst above 0.3 V_{RHE} (green line, Fig. 2) are generally ascribed to the continuous Ru-surface oxidation, which occurs up to the formation of bulk RuO_2 above 1.1 V_{RHE}.[23,52] Analogous oxidation features would be expected also for the Ru/TiO$_x$/C$^{as\text{-}synth.}$ catalyst that has not yet undergone any reductive heat treatment, but in this case all voltammetric features are strongly suppressed, despite the fact that the SMD of the Ru-NPs and thus the expected *ECSA* of the Ru/TiO$_x$/C$^{as\text{-}synth.}$ catalyst is essentially identical with that of the Ru/C catalyst. The origin of this difference is unclear and might be related to either remaining surface contaminants from the synthesis process, a very low conductivity of the amorphous TiO$_x$ particles, and/or a higher amount of surface oxidation of Ru in Ru/TiO$_x$/C$^{as\text{-}synth.}$. For the Ru/TiO$_x$/C$^{400°C,H_2}$ catalyst, the Ru surface oxidation is similarly suppressed, which could be the result of the ECSA loss due to particle sintering (yielding a ≈2-fold lower SMD), a reduced conductivity of TiO$_x$ at higher potentials,[36] or the desired SMSI effect.[34,35] The pronounced H_{upd}-like features below 0.3 V_{RHE} indicate that the reduced ECSA cannot be the sole reason for the reduced Ru surface oxidation currents above 0.3 V_{RHE} and that a significant change in the Ru surface chemistry must have occurred compared to the Ru/C reference following the reductive heat-treatment of the catalyst that resulted in the reduction of the Ru particles and the formation of an SMSI.

To further investigate the different oxidation behavior and obtain insights into the contributions of surface reduction and H_{upd} in the low potential region, each catalyst was cycled to a stepwise increasing upper cutoff potential from 0.6 up to 1.3 V_{RHE} (Fig. 3). For the Ru/C reference catalyst, the cycling is reversible up to an upper cutoff potential of 1.1 V_{RHE} (Fig. 3a). However, surpassing this upper potential limit, the surface passivation becomes irreversible, which is shown by the decreasing oxidative current in the anodic scan of the steady-state CVs, i.e., steady state CVs with a higher upper potential limit do not follow the anodic CVs of measurements with a lower upper potential limit even within that range. Simultaneously, the reduction feature that starts below ≈0.4 V_{RHE} during the cathodic scan are shifting to lower potentials with increasing upper potential limit, thus indicating that higher overpotentials are required to reduce the Ru-NPs again (indicated by the arrow in Fig. 3a).

In contrast, the Ru/TiO$_x$-based catalysts could be cycled to an upper potential limit of 1.3 V_{RHE} with significantly improved reversibility. While the Ru/TiO$_x$/C$^{as\text{-}synth.}$ catalyst showed a certain degree of irreversibility when cycled to 1.3 V_{RHE}, the reductive peak at ≈0.2 V_{RHE} does not shift to lower potentials. Thus, already by introducing a TiO$_x$ support, Ru could be stabilized in its metallic state up to high positive potential limits (Fig. 3b). This might be the result of an electrochemical SMSI formation by hydrogen spillover induced reduction or the TiO$_x$ support or the dissolution and subsequent redeposition of TiO$_x$ within the first 25 cleaning cycles.[35,37,54,55] The stabilization is more pronounced after an SMSI was formed (Fig. 3c). Here, the decreased surface oxidation
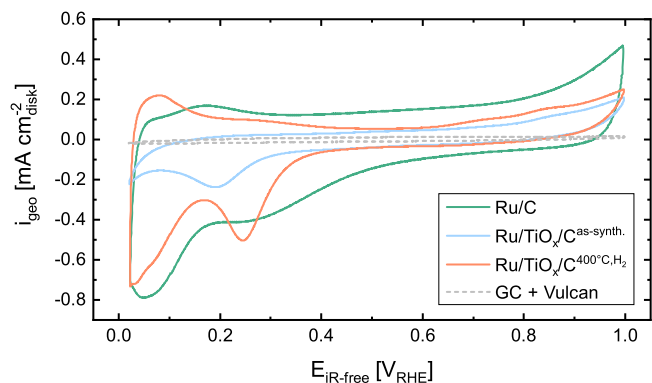

Figure 2. CVs of Ru/C (green), Ru/TiO$_x$/C$^{as\text{-}synth.}$ (blue), Ru/TiO$_x$/C$^{400°C,H_2}$ (orange), and the corresponding Vulcan-carbon baseline (gray dashed) in Ar-saturated 0.1 M HClO$_4$ at 0 rpm. All measurements were recorded in an RDE setup at 25 °C with a scan rate of 20 mV s^{-1}, a loading of 17 ± 2 μg_{Ru} cm$_{disk}^{-2}$ and an ionomer/support (C + TiO$_x$) ratio of I/S = 0.1. The potential was corrected for the HFR of the setup. The loading of the pure Vulcan carbon electrode was ≈45 μg_C cm$_{disk}^{-2}$ and thus closely matched that in the Ru/TiO$_x$/C catalysts.
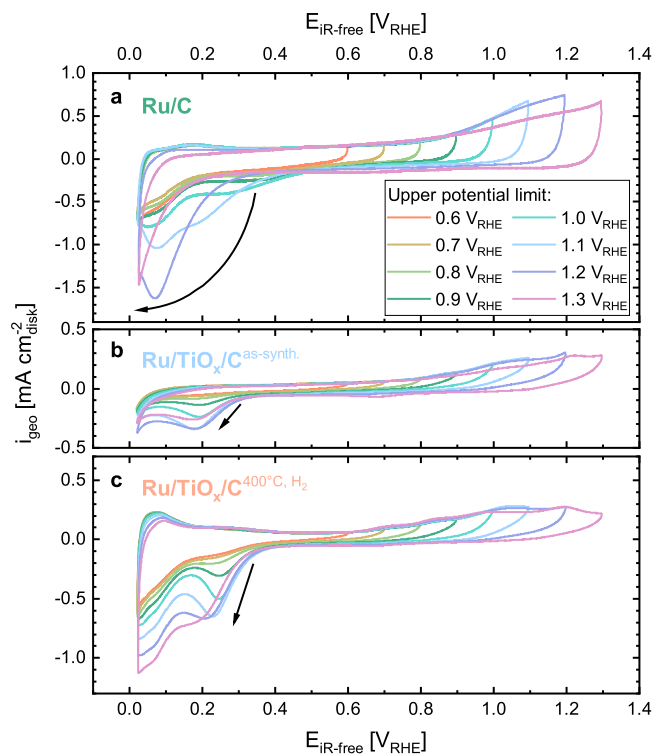
Figure 3. Steady state CVs of the various catalysts in Ar-saturated 0.1 M HClO$_4$ with increasing upper potential limits: (a) Ru/C; (b) Ru/TiO$_x$/C$^{as\text{-}synth.}$; and (c) Ru/TiO$_x$/C$^{400°C,H_2}$ recorded. All measurements were recorded at 25 °C, in an RDE setup at 0 rpm with a scan rate of 20 mV s^{-1}, a Ru loading of 17 ± 2 μg_{Ru} cm$_{disk}^{-2}$, and an ionomer/support (C + TiO$_x$) ratio of I/S = 0.1; the potentials were corrected for the HFR of the setup.

of Ru was found fully reversible, whereby the reduction feature at ≈0.25 V_{RHE} does not exhibit a negative shift except for the highest upper cutoff potential of 1.3 V_{RHE}, where a negative shift of ≈20 mV could be observed. At low potentials (<0.3 V_{RHE}), the Ru/TiO$_x$/C$^{400°C,H_2}$ catalyst clearly features a mixed region, where H_{upd} (indicated by the positive currents in the anodic scan that are missing in the other catalysts), Ru oxide reduction, and the onset of the HER overlap.
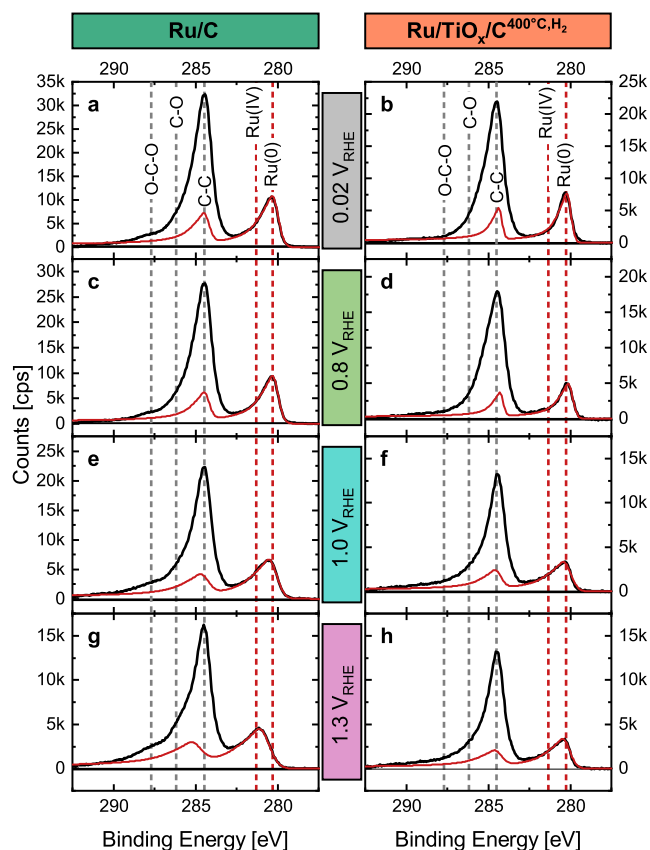
Figure 4. XPS of Ru/C (left) and Ru/TiO$_x$/C$^{400°C,H_2}$ (right) drop-casted on a gold foil and polarized in 0.1 M HClO$_4$ at different potentials for 600 s: (a) and (b) 0.02 V$_{RHE}$; (c) and (d) 0.8 V$_{RHE}$; (e) and (f) 1.0 V$_{RHE}$; and, (g) and (h) 1.3 V$_{RHE}$. The catalysts were reduced at 0.02 V$_{RHE}$ for 600 s before being exposed to oxidative potentials. Due to an overlap with the C 1s peaks (only peak positions indicated for clarity), the Ru 3d$_{3/2}$ peak was fixed to the 3d$_{5/2}$ peak and the doublet was jointly fitted (red lines, details see experimental section). The black lines mark the total measured XPS counts.

Oxidation state analysis by XPS.—To get more insight into the Ru (surface) oxidation behavior of the Ru/C and the Ru/TiO$_x$/C$^{400°C,H_2}$ catalysts, they were pre-polarized at 0.02, 0.8, 1.0, and 1.3 V$_{RHE}$ in 0.1 M HClO$_4$ for 600 s, then emersed from the electrolyte, dried, and finally examined by XPS. To ensure that the oxidation state of the Ru-NPs is due to the effect of the oxidation potential rather than the storage conditions before conducting these experiments, a 600 s hold at 0.02 V$_{RHE}$ was implemented prior to any oxidative polarization (for details see experimental section). While XPS is technically a surface sensitive technique with a penetration depth of ≈3 nm for a kinetic energy of ≈1200 eV of the photo electrons (i.e., in the R 3d region using an Al X-ray source),[56] the small particle size of the Ru-NPs implies that the XPS signal comprises a major contribution from the bulk of the Ru-NPs particles in addition to their surface. Although the Ru 3d$_{3/2}$ signal overlaps with the main C 1s feature from the Vulcan carbon support (at 284.4 eV[47]), the stronger Ru 3d$_{5/2}$ peak is located at sufficiently low binding energy so that it does not overlap with the C 1s feature. Note that the Ru 3p$_{3/2}$ signal (461.7–463.2 eV, depending on the oxidation state)[46] overlaps completely with the much stronger Ti 2p features (Ti(IV)$_{3/2}$ at 458.5 and Ti(IV)$_{1/2}$ at 464.2 eV, data not shown), so that this spectral region was not considered and the following XPS analysis is focusing on the Ru 3d region (for details see Table II).

Thus, Fig. 4 shows the Ru 3d XPS spectra of the Ru/C (left) and the Ru/TiO$_x$/C$^{400°C,H_2}$ (right) catalysts after polarization. After emersion at the lowest potential of 0.02 V$_{RHE}$, the Ru 3d$_{5/2}$ peaks
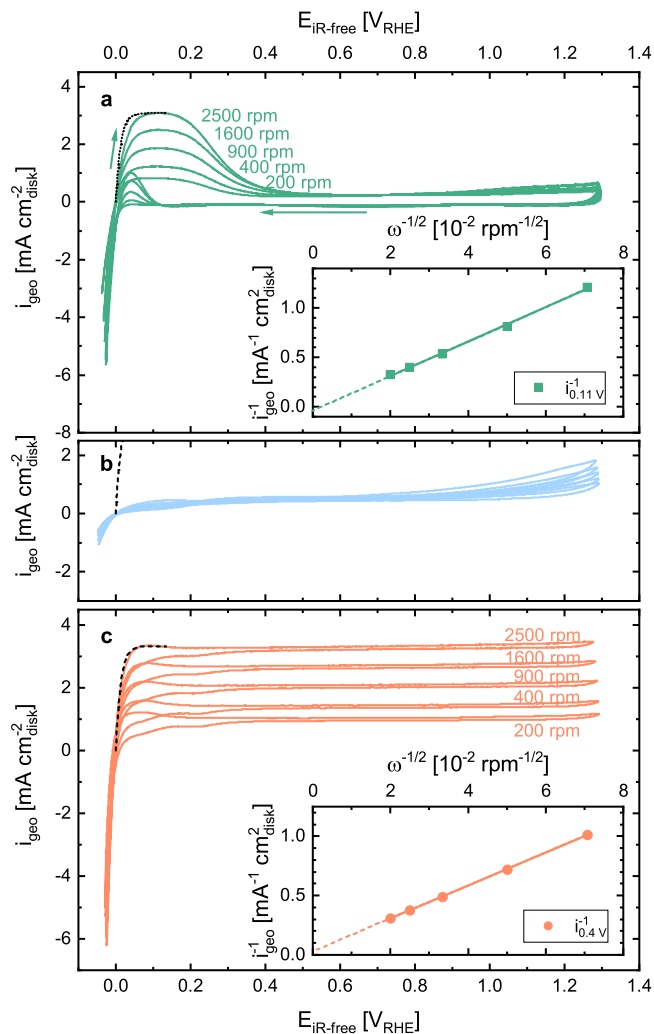
Figure 5. Rotation rate dependent HER/HOR polarization curves in H$_2$-saturated 0.1 M HClO$_4$ at 25 °C: (a) Ru/C; (b) Ru/TiO$_x$/C$^{as-synth.}$; (c) Ru/TiO$_x$/C$^{400°C,H_2}$. All measurements were recorded in an RDE setup at a scan rate of 20 mV s^{-1}, with a loading of 17 ± 2 μg$_{Ru}$ cm$_{disk}^{-2}$ and an ionomer/support (C + TiO$_x$) ratio of I/S = 0.1, and were corrected for the HFR of the setup. The dashed black lines represent the pure Nernstian diffusion overpotentials for the positive-going scan at 2500 rpm. The insets show Koutecký-Levich plots of the inverse of the current density vs the inverse square root of the electrode rotation speed ω: in (a) for the Ru/C catalyst at the current maximum, taken at 0.11 V$_{RHE}$; in (c) for the Ru/TiO$_x$/C$^{400°C,H_2}$ catalyst at the stable plateau, taken at 0.4 V$_{RHE}$.

at 280.3 eV for Ru/C (Fig. 4a) and 280.2 eV for Ru/TiO$_x$/C$^{400°C,H_2}$ (Fig. 4b) correspond to Ru(0), thus confirming that the Ru-NPs are fully reduced to metallic Ru at this potential.[46] After the polarization at 0.8 V$_{RHE}$, the spectra remain essentially identical (Fig. 4c and d), although a partial oxidation of the Ru surface would have been expected for the Ru/C catalyst based on its CV (green line in Fig. 2). This might be the result of a reversible hydroxide adsorption by water discharge at these potentials,[52] whereby no stable oxide is formed and the majority of Ru atoms therefore remain in metallic state after vacuum drying of the sample. After polarization at 1.0 V$_{RHE}$, a small peak shift of 0.2 eV to higher binding energies was detectable for both catalysts, which might indicate partial oxidation of Ru (Figs. 4e and 4f), as would be expected from the CV measurements (see Figs. 3a and 3c). After polarization to 1.3 V$_{RHE}$, the Ru-NPs of the Ru/C reference are largely oxidized, as is indicated by a peak shift to 281.2 eV (corresponding to Ru(IV), Fig. 4g), while the Ru-NPs of the Ru/TiO$_x$/C$^{400°C,H_2}$ catalyst still show the the characteristic Ru(0) peak at 280.2 eV (Fig. 4h). These
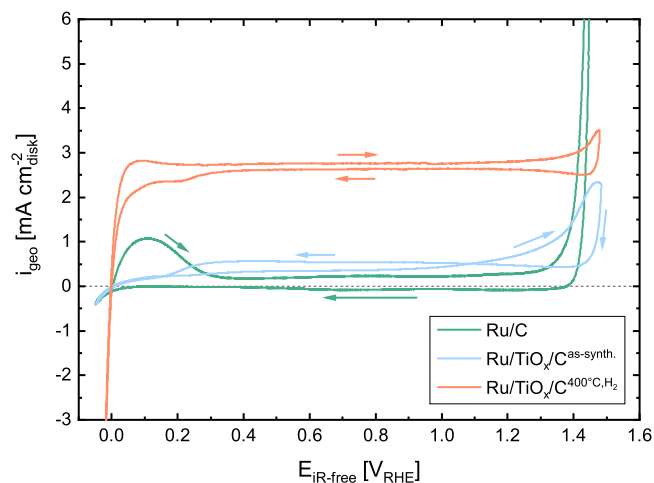
Figure 6. HER/HOR polarization curves in H_2-saturated 0.1 M $HClO_4$ at 1600 rpm and 25 °C that are extended into the OER potential window of the Ru/C (green), the Ru/TiO$_x$/C$^{as-synth.}$ (blue), and the Ru/TiO$_x$/C$^{400°C,H_2}$ (orange) catalysts. All measurements were recorded after the rotation rate dependent HER/HOR polarization curves under identical conditions (see Fig. 5).

results confirm the observations from the CV measurements that Ru oxidation is significantly suppressed for the Ru/TiO$_x$/C$^{400°C,H_2}$ compared to the Ru/C reference catalyst. Whether this stabilization is the result of a TiO$_x$ encapsulation could unfortunately not be verified by investigating the Ti 2p spectrum, as the fraction of Ti in such a thin film would have an insignificant contribution compared to the bulk TiO_2 of the support structure. No changes in the Ti 2p spectrum could therefore be observed, except for a potential dependent shift of the shoulder corresponding to the Ru 3p$_{3/2}$ signal (data not shown).

HER/HOR investigation by RDE.—In the case of similarly prepared Pt/TiO$_x$/C$^{400°C,H_2}$ catalysts, the analogously observed suppression of the surface oxide formation was accompanied by an extension of the HOR activity of Pt to very high positive potentials.[35] Therefore, we will next examine whether this will also hold true for the Ru/TiO$_x$/C$^{400°C,H_2}$ catalyst, using RDE experiments at different rotation rates in 0.1 M $HClO_4$. For the Ru/C reference catalyst, a high HER activity is observed, but its HOR activity quickly decreases above 0.15 V$_{RHE}$ due to surface oxidation (Fig. 5a), analogous to what had been observed for a ruthenium metal disk.[23] A Koutecký-Levich analysis relating the reciprocal current density maximum (at 0.11 V$_{RHE}$) and the inverse square root of the rotation rate shows an essentialy zero y-axis intercept, thus confirming that the HOR currents are mostly mass-transport limited at 0.11 V$_{RHE}$ (Fig. 5a inset). However, when comparing the actual oxidation currents below 0.11 V$_{RHE}$ with those predicted by the purely Nernstian diffusion overpotential for HOR[57] for the positive-going scan at 2500 rpm (see dashed black line in Fig. 5a), it becomes clear that the HOR on the Ru/C catalyst in this region is still affected by kinetic limitations. As the potential reaches ≈0.5 V$_{RHE}$ during the positive-going scan, the HOR activity of the Ru-NPs has vanished to zero, and only once the Ru surface is polarized again below 0.1 V$_{RHE}$ during the negative-going scan, some HOR activity can again be observed. The HER activity at negative potentials is sufficiently good to reach a mostly mass-transport controlled current profile that is expected for highly active HER catalysts in acidic RDE measurements.[58]

As discussed previously, the Ru/TiO$_x$/C$^{as-synth.}$ catalyst appeared to suffer from a poor conductivity and/or from poisoning by surface adsorbates from the synthesis, which also seems limit its ability to

oxidize hydrogen (Fig. 5b). Independent on the rotation rate, the catalyst showed almost no HOR activity and never reached the mass-transport limited current densities. Since any residual organic surface contaminations would be expected to be oxidized upon cycling to 1.3 V$_{RHE}$ multiple times but the HOR performance did not increase, it is more likely that the suppressed HOR activity is the result of the poor conductivity of the as-synthesized TiO$_x$ that results in most of the Ru particles being electrically insulated.

In contrast to the Ru/C catalyst, the polarization curve of the Ru/TiO$_x$/C$^{400°C,H_2}$ catalyst shows a steady HOR activity up to 1.3 V$_{RHE}$ (Fig. 5c). The zero y-axis intercept in the Koutecký-Levich analysis at 0.4 V$_{RHE}$ (to exclude H$_{upd}$ contributions) shows that even at higher potentials, the currents are purely mass-transport limited (Fig. 5c inset). In contrast to the Ru/C catalyst, the HOR currents of the Ru/TiO$_x$/C$^{400°C,H_2}$ catalyst are now exclusively limited by the Nernstian diffusion overpotential (black dashed line in Fig. 5c) rather than kinetics, which means its true HOR kinetics cannot be assessed by RDE measurements (see below for kinetic investigation in an MEA setup).[57]

Since the SMSI in Ru/TiO$_x$/C$^{400°C,H_2}$ prevents the (surface) oxidation of Ru and thereby enables continuous hydrogen oxidation even at 1.3 V$_{RHE}$, it will likely also impact the OER performance of the catalyst, as was observed for a Pt/TiO$_x$ based catalyst.[34] Thus, the OER activity of the Ru/C, Ru/TiO$_x$/C$^{as-synth.}$, and Ru/TiO$_x$/C$^{400°C,H_2}$ catalysts was examined by extending the upper potential limit in the HER/HOR polarization curves to 1.5 V$_{RHE}$ (Fig. 6). The OER on the Ru/C reference catalyst readily starts above 1.3 V$_{RHE}$, as shown by the steep current increase. As these measurements had been performed after the HER/HOR polarization curves at different rotation rates up to 1.3 V$_{RHE}$, the HOR activity of Ru/C has already severely degraded compared to the initial experiments shown in Fig. 5. This limited stability of Ru in acidic environment is well known and Ru dissolution poses a major issue for the implementation of any Ru containing catalyst in PEMFCs and similar systems.[59,60] The mass-transport limited current density was therefore not reached anymore even in the first scan. After the catalyst had been exposed to even higher potentials of 1.5 V$_{RHE}$, the overpotential for Ru reduction apparently has shifted to even more negative potentials, continuing the trend observed in Fig. 3a and thereby nearly completely deactivating the HER activity of the Ru/C catalyst. In contrast, the Ru/TiO$_x$/C$^{400°C,H_2}$ catalyst maintains its superior HOR activity as well as its high HER activity when polarized up to 1.5 V$_{RHE}$, but its OER activity is strongly suppressed, as is indicated by the observation that the current upper potential limit of 1.5 V$_{RHE}$ barely exceeds the HOR current plateau. This observation and the fact that the HER/HOR activity is maintained even after harsh oxidative potentials confirm the successful stabilization of Ru in its metallic state. The OER activity of the Ru/TiO$_x$/C$^{400°C,H_2}$ catalyst still exceeds that of a similarly stabilized Pt/TiO$_x$/C$^{400°C,H_2}$ catalyst,[35] which is most likely the result of a small fraction of Ru-NPs that are located on the carbon support and thus are not affected by the SMSI effect. While the HOR activity of Ru/TiO$_x$/C$^{as-synth.}$ remained almost completely suppressed, the catalyst showed a surprisingly high activity for the OER that by far exceeded that of the heat-treated catalyst. These observations confirms that the stabilization of Ru against (surface) oxidation is indeed the result of an encapsulation of the Ru particles due to SMSI effects after the reductive heat-treatment, thereby enabling a high HOR activity at potentials where surface passivation by (surface) oxide formation would otherwise have occurred.

CV characterization of the catalysts in MEAs.—As the HER/HOR rates on platinum group metal catalysts with high HOR/HER activity (e.g., Pt or Ir) cannot be determined precisely in acidic liquid electrolyte using an RDE setup,[57] the HER/HOR kinetics of the Ru/TiO$_x$/C$^{400°C,H_2}$ catalyst (and of the Ru/C catalyst as a reference) were investigated using a PEMFC-based hydrogen pump approach,
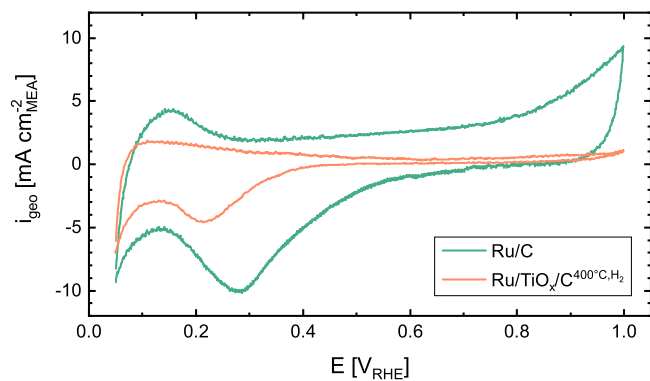
Figure 7. Cyclic voltammograms of Ru/C (green, 56 μg_{Ru} cm$_{MEA}^{-2}$) and Ru/TiO$_x$/C$^{400°C,H_2}$ (orange, 44 μg_{Ru} cm$_{MEA}^{-2}$) working electrodes recorded in a 5 cm^2 single-cell PEM fuel cell at a scan rate of 100 mV s^{-1} from 0.05 to 1.0 V$_{RHE}$ at ambient pressure and 40 °C. The CE compartment was purged with 200 nccm 5% H$_2$/Ar (humidified at 90% RH), while the WE compartment was purged with 50 nccm dry N$_2$ (set to zero flow when recording the CV).
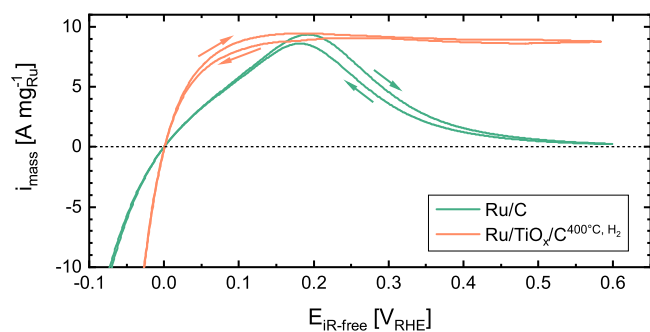
Figure 8. Mass normalized potentiodynamic HER/HOR polarization curves at 5 mV s^{-1} on the Ru/C (green) and Ru/TiO$_x$/C$^{400°C,H_2}$ (orange) catalyst in a 5 cm^2 single-cell PEMFC, with the potential corrected for the HFR at OCV (E$_{iR-free}$). The data were recorded at 80 °C, 100 kPa$_{H_2}$, 90% RH and 2000/2000 nccm H$_2$ (through the WE/CE compartments). Electrode loadings of the MEAs: 56 μg_{Ru} cm$_{MEA}^{-2}$ for the Ru/C WE and 44 μg_{Ru} cm$_{MEA}^{-2}$ for the Ru/TiO$_x$/C$^{400°C,H_2}$ WE; the Pt loading of the Pt/C CE was 0.39 ± 0.02 mg$_{Pt}$ cm$_{MEA}^{-2}$.

where much higher H$_2$ mass-transport rates can be achieved.[25] Figure 7 compares the CVs of the Ru/C (green line) and Ru/TiO$_x$/C$^{400°C,H_2}$ (orange line) catalysts as working electrode (WE) in an MEA (with a Pt/C counter electrode (CE)), obtained in a 5 cm^2 single-cell, with the WE held under N$_2$ and the CE compartment purged with humidified 5% H$_2$/Ar. While the Ru/C CV is very similar to that recorded in Ar-saturated 0.1 M HClO$_4$ (Fig. 2), with similar oxidative and reductive features, the voltammetric currents of the Ru/TiO$_x$/C$^{400°C,H_2}$ catalyst measured in the MEA are only similar to those obtained in the 0.1 M HClO$_4$ electrolyte in the hydrogen adsorption/desorption region, but almost vanish at potentials above ≈0.5 V$_{RHE}$. This could be the result of several factors. First, the liquid electrolyte in the RDE setup might access the Ru surface better than the ionomer, especially when Ru is supported and encapsulated by TiO$_x$. It has frequently been observed that the ECSA determined by RDE differs from that observed for the same catalyst in an MEA,[57,61] and it is likely that this effect will be more pronounced for a catalyst with a more complex structure like that of the Ru/TiO$_x$/C$^{400°C,H_2}$ catalyst. Secondly, the interaction of the two support materials with the ionomer might be different, causing the ionomer to adsorb preferentially on either C or TiO$_2$,[62,63] thus leading to selective electrochemical accessibility of Ru particles being supported on either of the support materials. In either case, it is

clear that the difference in Ru loading (44 μg_{Ru} cm$_{MEA}^{-2}$ for Ru/TiO$_x$/C$^{400°C,H_2}$ compared to 56 μg_{Ru} cm$_{MEA}^{-2}$ for Ru/C) is too small to result in such different CVs, especially considering that the H$_{upd}$ features of Ru/TiO$_x$/C$^{400°C,H_2}$ (orange line, Fig. 7) are significantly enhanced compared to the overall capacitive currents.

H$_2$-pump measurements in a single-cell PEMFC configuration.—In a first set of experiments to determine the HER/HOR mass activity of the catalysts, CVs were recorded potentiodynamically at 5 mV s^{-1} in a H$_2$–pump configuration, scanning the potential from -0.3 to 0.6 V$_{RHE}$ (Fig. 8). Again, the Ru/C catalyst (green line) strongly deactivates above 0.2 V$_{RHE}$, whereas the Ru/TiO$_x$/C$^{400°C,H_2}$ (orange line) catalyst maintains its activity up to the highest investigated potential of 0.6 V$_{RHE}$. Although the H$_{upd}$ features in Fig. 7 indicated less ECSA for the Ru/TiO$_x$/C$^{400°C,H_2}$ catalyst, its HER/HOR activity at low overpotentials (⩽30 mV) by far outperforms that of the Ru/C reference catalyst. For the HOR on the Ru/TiO$_x$/C$^{400°C,H_2}$ the performance curve quickly deviates from the expected Butler-Volmer behavior and reaches a current plateau of ≈9 A mg$_{Ru}^{-1}$ (corresponding to ≈0.4 A cm^{-2}$_{MEA}$) at high overpotentials above ≈0.2 V$_{RHE}$. For Pt catalysts, similar limitations in current density have been discussed to be due to a change from a rate determining Volmer-step to a Tafel-limited[25,57,64,65] or a Heyrovsky-limited step,[66] or due to a hydrogen mass-transport limitation through the ionomer film covering the catalyst surface.[25] In the latter case, the specific current density at which mass transport resistances through the ionomer film could be limiting was estimated to be ≈2 A cm$_{Pt}^{-2}$ for a Pt/C catalyst.[25] Based on the *ECSA* of ≈110 m^2 g$_{Ru}^{-1}$ that can be estimated from the measured SMD of ≈4.4 nm (using the spherical approximation) and the Ru loading of 44 μg_{Ru} cm$_{MEA}^{-2}$, the Ru roughness factor of the Ru/TiO$_x$/C$^{400°C,H_2}$ catalyst can be estimated to be ≈50 cm$_{Ru}^{-2}$ cm$_{MEA}^{-2}$, which then would convert to a limiting specific current density of ≈8 mA cm$_{Ru}^{-2}$ for the data in Fig. 8. As this is nearly three orders of magnitude lower than the expected mass transport limitation near a specific current density of ≈2 A cm$_{Ru}^{-2}$, mass-transport resistances through the ionomer film can be ruled out as the origin of the current plateau observed in Fig. 8. However, an encapsulation of Ru, as it was discussed above and has been suggested for similar oxide supported Pt catalysts,[32,34,35,37] might be another source for a significant local hydrogen transport resistance to the active site. This hypothesis is supported by a suppressed chemisorption of hydrogen that has been reported for a SMSI between Ru and TiO$_2$.[67]

On the other hand, in the case of a limitation by a rate determining adsorption step, the current limitation would be given by the rate of adsorption, whereby the current plateau of only 9 A mg$_{Ru}^{-1}$ could result from slow hydrogen adsorption kinetics on the Ru surface. In the case of Pt, an adsorption rate constant of ≈2.4 cm s^{-1} at 22 °C determined from H$_2$-D$_2$ exchange experiments by Vogel et al. would predict a limiting specific current density of ≈0.40 A cm$_{Pt}^{-2}$ at 100 kPa$_{H_2}$,[25,68] i.e., of the same order of magnitude as the estimated transport limiting current density through the ionomer film (see above), so that for a Pt catalyst the observed limiting current may originate from either kinetic or local transport limitations (or both). To the best of our knowledge there is only the study by Lu et al. that reports a hydrogen adsorption rate constant for Ru, but only states that it exceeds their detection limit of 10^{-3} cm s^{-1} at 25 °C (H$_2$-D$_2$ exchange experiments).[69] If the hydrogen adsorption rate were to be responsible for the specific current density limitation of ≈8 mA cm$_{Ru}^{-2}$ observed in Fig. 8 (see above), it would have to be on the order of 10^{-2} cm s^{-1}.

Since the current density maximum reached by the Ru/C reference catalyst (green line, Fig. 8) coincides with that of the Ru/TiO$_x$/C$^{400°C,H_2}$ catalyst (orange line, Fig. 8), a distinction between a Ru-specific limitation and a limitation induced by the interaction of Ru and TiO$_x$ is not possible at this point. Still, it is most likely that the equal mass normalized current density maximum
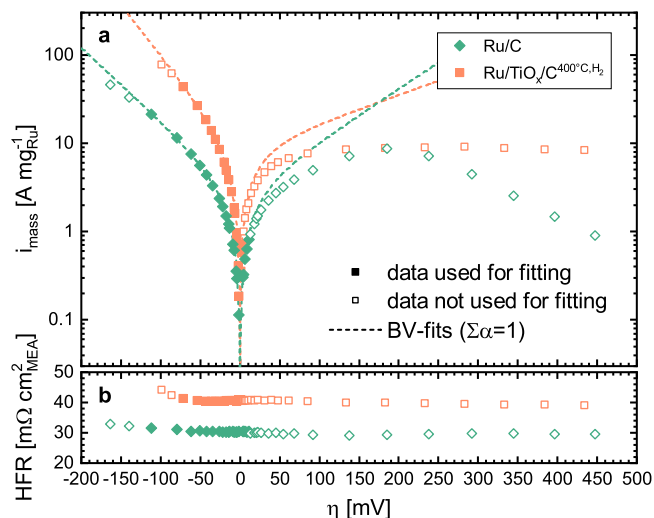
Figure 9. Mass normalized kinetic current densities for the HER/HOR (a) and corresponding HFRs (b) of representative MEAs of with Ru/C (green) and Ru/TiO$_x$/C$^{400°C,H_2}$ (orange) WEs, recorded by a combination of galvanostatic/potentiostatic measurements (all data at 80 °C, 90% RH, 100 kPa$_{H_2}$, and 2000/2000 nccm H$_2$). The overpotential η was calculated from the HFRs according to Eq. 4. The data points used (filled symbols) and excluded (open symbols) for the shown Butler-Volmer fits (dashed lines) represent the average over the last 10 s of a 60 s galvanostatic/potentiostatic hold period (see Experimental section). The selection criteria for data to be included in the Butler-Volmer fits are: (i) a less than 1 mΩ cm$_{MEA}^2$ HFR increase for the HER data; (ii) a current density of less than 10% of the maximum current density for the HOR data. Furthermore, the sum of the transfer coefficients in Eq. 6 was fixed to one (i.e., $\alpha_a + \alpha_c = 1$). Electrode loadings of the MEAs: 56 μg$_{Ru}$ cm$_{MEA}^{-2}$ for the Ru/C WE and 44 μg$_{Ru}$ cm$_{MEA}^{-2}$ for the Ru/TiO$_x$/C$^{400°C,H_2}$ WE; the Pt loading of the Pt/C CE was 0.39 ± 0.02 mg$_{Pt}$ cm$_{MEA}^{-2}$.

is a coincidence rather than an intrinsic property of the Ru catalysts, as the MEA roughness factors of the two Ru catalysts differ by a factor of ≈2.5 (due to the differences in Ru loading and the Ru-NP SMD), which means that the estimated specific limiting current density maximum also differs by the same factor, while hydrogen adsorption limitations would be expected to scale with the specific current density. In any case, the currents of the Ru/C reference decrease drastically with increasing potential after having reached the maximum current density at ≈0.2 V$_{RHE}$, whereby the catalyst deactivates almost completely upon reaching 0.4 V$_{RHE}$. On the contrary, the current density plateau is maintained up to 0.6 V$_{RHE}$ for the stabilized Ru/TiO$_x$/C$^{400°C,H_2}$.

For a more accurate determination of the HER/HOR kinetics, a steady-state approach was chosen to avoid time dependent artifacts such as HFR variations due to membrane dry-out.[25] HER/HOR polarization curves were recorded using a static measurement approach that allows for the system to equilibrate at each point, whereby the HFR is determined by EIS directly after every hold period (Fig. 9). The HFRs of all MEAs with Ru/TiO$_x$/C$^{400°C,H_2}$ (orange symbols, Fig. 9b) were roughly 10 mΩ cm$_{MEA}^2$ higher than of MEAs with Ru/C (green symbols, Fig. 9b). As differences in electrode thickness were accounted for when assembling the cells, contact resistances can most likely be ruled out as the origin of this offset. Instead, ionic contamination from TiO$_2$ dissolution might be the cause for the slightly higher HFR of the MEAs with the Ru/TiO$_x$/C$^{400°C,H_2}$ catalyst, as according to the Pourbaix diagram (given for 25 °C), bulk TiO$_2$ has a low but finite solubility of ≈10^{-8} mol l^{-1} at pH 0 (the approximate pH of a PFSA membrane) at the negative iR-free potential limit of −0.2 V$_{RHE}$ that was used in these H$_2$-pump experiments;[70] considering that the solubility will likely be higher at 80 °C and for the nano-sized TiO$_x$ support, a

significant dissolution of titanium species is quite plausible. While low concentrations of cation contamination would reduce the membrane conductivity without severely affecting the performance, higher concentrations would lead to significant voltage losses in the system.[71,72] Furthermore, the detrimental effect of TiO$_2$ on the long term durability of PEMFC systems has recently been shown by Zhang et al.,[73] which limits the overall applicability of the here presented catalyst system and might require the use of a more stable oxide support that still develops an SMSI, such as tungsten oxide.[74,75]

With the differences in HFR accounted for according to Eq. 4, a representative dataset of the mass normalized kinetic HER/HOR currents obtained from the static measurement approach is depicted in the form of a Tafel plot in Fig. 9a for the Ru/TiO$_x$/C$^{400°C,H_2}$ catalyst and for the Ru/C reference catalyst. Both the anodic and cathodic branches of the Tafel plots show a behavior according to the Butler-Volmer equation (Eq. 6) at low overpotentials:[44,76]

$$i_{kin} = i_0 \cdot \left(e^{\frac{\alpha_a F \eta}{RT}} - e^{\frac{-\alpha_c F \eta}{RT}} \right) \quad [6]$$

with i_{kin} being the kinetic current density in A mg$_{Ru}^{-1}$, i_0 the exchange current density in A mg$_{Ru}^{-1}$, α_a/α_c the anodic/cathodic transfer coefficients, η the overpotential in V (i.e., the difference between the potential and the equilibrium potential), F the Faraday constant (96,484 A s mol^{-1}), R the universal gas constant (8.314 kJ mol^{-1} K^{-1}), and T the temperature in K. While the HER part was seemingly unlimited over the complete potential interval, the HOR currents reached the same maximum value that was observed in the potentiodynamic experiments (see Fig. 8), whereby the HOR activity of the Ru/C reference catalyst (green symbols) rapidly decreased above an HOR overpotential of ≈0.2 V, while the Ru/TiO$_x$/C$^{400°C,H_2}$ catalyst (orange symbols) maintained this maximum activity up to highest measured overpotential of 0.45 V.

The exchange current density i_0 has been obtained by fitting the data to the Butler-Volmer equation with a sum of transfer coefficients of one ($\alpha_a + \alpha_c = 1$, dashed lines), representing a predominant Tafel-Volmer mechanism that is most often assumed for platinum group metals.[57,76–79] According to our established protocol,[25] exclusively data points with currents of less than 10% of the current maximum were fitted to minimize the effect of the HOR current limitation on the kinetic evaluation, and all data points with an HFR increase of more than 1 mΩ cm$_{MEA}^2$ (compared to the average HFR in the overpotential range of ±20 mV) were excluded for fitting in order to ensure that the correction of the potential for the Ohmic drop was accurate under the relevant measurement conditions. Data points considered for fitting are depicted as full symbols, whereas data points that were excluded from the fits are depicted as open symbols in Fig. 9. While the fit for the Ru/C catalyst (green line, Fig. 9a) showed a high degree of symmetry, the Ru/TiO$_x$/C$^{400°C,H_2}$ catalyst (orange line, Fig. 9a) seems to be severely affected by the HOR limitation already at low overpotentials (⩽30 mV), resulting in highly asymmetrical fits with α_a-values of 0.26 ± 0.03. An analogous behavior has previously been observed for a carbon supported Pt catalyst, where it was not possible to determine whether the observed limiting HOR current is due to an intrinsic kinetic effect or due to H$_2$ mass transport restrictions through the ionomer film.[25] For the ≈50-fold lower limiting current when evaluated in terms of specific current density in the case of the Ru/TiO$_x$/C$^{400°C,H_2}$ catalyst (≈8 mA cm$_{Ru}^{-2}$ vs ≈400 mA cm$_{Pt}^{-2}$ in the case of Pt/C, as discussed above), a limitation by H$_2$ transport can be excluded, so that it must be due to a kinetic limitation (e.g., by hydrogen adsorption/dissociation).

The exchange current densities at 80 °C determined from the Butler-Volmer fits (dashed lines in Fig. 9), are roughly three times higher for the Ru/TiO$_x$/C$^{400°C,H_2}$ catalyst (i_0 = 8.2 ± 0.3 A mg$_{Ru}^{-1}$) compared to the Ru/C reference catalyst (i_0 = 2.5 ± 0.2 A mg$_{Ru}^{-1}$).

Thus, the exchange current density of the $Ru/TiO_x/C^{400°C,H_2}$ catalyst is similar to those of Rh/C and Pd/C (both ≈ 15 A mg_{metal}^{-1} for the catalysts studied by Durst et al.[57]), but roughly two orders of magnitude lower than for Pt/C ($i_0 = 540 \pm 160$ A mg_{Pt}^{-1})[25] under the same conditions. Consequently, loadings of ≈ 1 mg_{Ru} cm_{MEA}^{-2} would be required to limit the HER/HOR overpotentials to <10 mV at 2 A cm^{-2} in a PEMFC or PEMWE, while this can be achivieved with the currently used Pt/C catalysts for loading of <0.05 mg_{Pt} cm_{MEA}^{-2}. These high loadings annihilate the cost advantage of Ru compared to conventional Pt catalysts for the hydrogen side of PEM systems.

Conclusions

In this study, an HOR active $Ru/TiO_x/C$ catalyst was synthesized via a multi-step synthesis route and subsequent reductive heat-treatment. According to tomographic TEM imaging, the catalyst consists mostly of agglomerated Ru/TiO_x-composites adsorbed on the Vulcan carbon support structure. The heat-treatment of the catalyst ($Ru/TiO_x/C^{400°C,H_2}$) leads to severe sintering of the Ru nanoparticles (Ru-NPs), increasing their Sauter mean diameteter (SMD) from 2.0 to 4.4 nm, and results in an increased crystallinity of the TiO_x support, accompanied by a partial encapsulation of the Ru particles due to strong metal support interaction (SMSI).

It was shown by cyclic voltammetry that Ru oxidation was suppressed for the $Ru/TiO_x/C^{400°C,H_2}$ catalyst compared to a Ru/C reference catalyst. This stabilization of Ru in its metallic state at high positive potentials was confirmed by XPS, whereby the Ru $3p_{5/2}$ peak remained at the binding energy of Ru(0) even after polarization at 1.3 V_{RHE} of the $Ru/TiO_x/C^{400°C,H_2}$ catalyst, while the Ru/C reference catalyst was fully oxidized to Ru(IV).

In RDE experiments, the $Ru/TiO_x/C^{400°C,H_2}$ catalyst showed an excellent stabilization of the HOR activity up to the onset of the OER at 1.3 V_{RHE}, whereas the HOR activity of the Ru/C reference quickly deactivated after reaching the mass-transport limited current density at 0.11 V_{RHE}. This stabilization of metallic Ru by SMSI resulted in a suppression of the OER activity above 1.3 V_{RHE}, where the Ru/C reference catalyst. outperformed the heat-treated catalyst, with Ru/C exhibiting by far the highest OER activity.

The HER/HOR kinetics of the catalysts were determined by PEMFC-based hydrogen-pump measurements. These confirmed the stabilization of the HOR activity of the $Ru/TiO_x/C^{400°C,H_2}$ catalyst, whereby at an overpotential of ≈ 0.1 V a maximum HOR current plateau of ≈ 9 A mg_{Ru}^{-1} was reached and maintained up to an overpotential of ≈ 0.45 V. This limiting current can clearly be ascribed to a kinetic limitation. With an exchange current density of 8.2 ± 0.3 A mg_{Ru}^{-1}, the $Ru/TiO_x/C^{400°C,H_2}$ catalyst proved to be three times more active than Ru/C (2.5 ± 0.2 A mg_{Ru}^{-1}), but roughly two orders of magnitude less active than Pt/C under the same conditions. In summary, it was shown that Ru can be stabilized for the HER/HOR by an SMSI, but the low activity and limited stability of both Ru and TiO_2 prevent this type of catalyst from representing a feasible alternative to conventional Pt/C catalysts.

Appendix

For TEM/EDX mappings, $Ru/TiO_x/C^{400°C,H_2}$ was dispersed in ethanol and drop-coated on a copper grid covered with a holey carbon film. STEM measurements were carried out on a probe corrected FEI Titan Themis operated at 300 kV in high-angle annular dark-field (HAADF) mode. Elemental maps were acquired with a Super-X energy-dispersive X-ray spectrometer and processed using the Velox V 3.0 software.
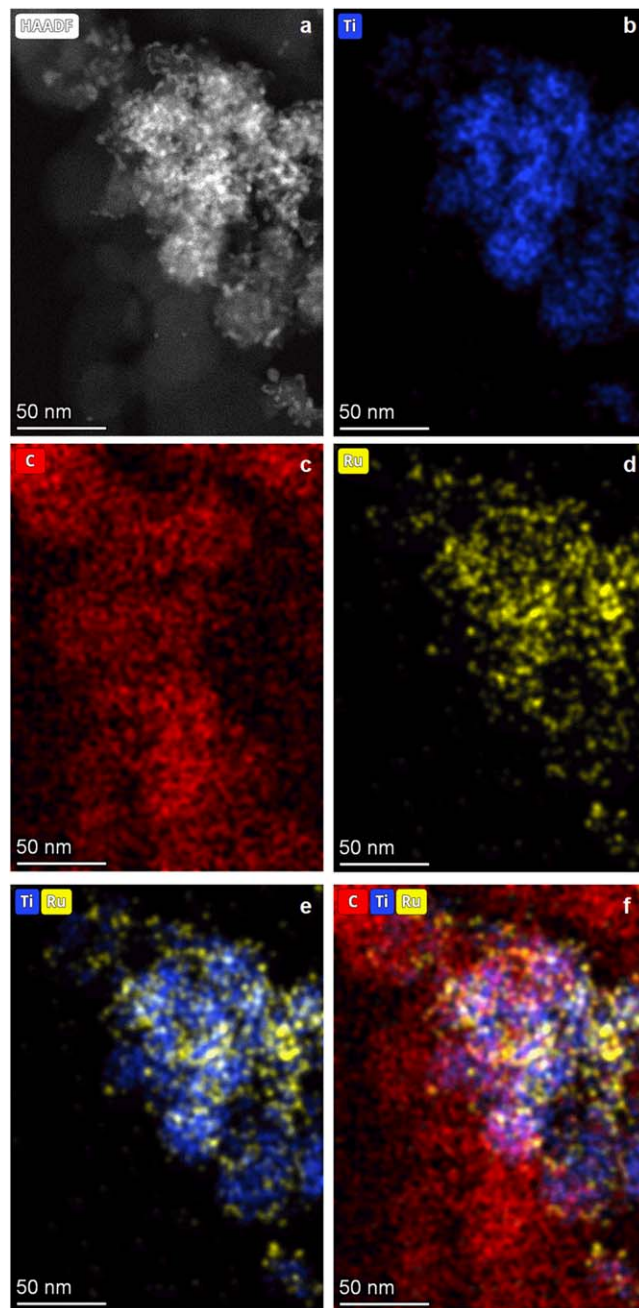
Figure A·1. Combined HAADF-STEM image and EDX mapping of the $Ru/TiO_x/C^{400°C,H_2}$ catalyst. Elements with a higher atomic number appear brighter in the HAADF image (a). The EDX mapping illustrates the location of Ti (b), C (c), Ru (d), and the combined locations of Ti and Ru (e), and C, Ti, and Ru (f), respectively. The combined EDX mappings clearly show that most of the Ru nanoparticles are located on TiO_x, whereas the carbon is mostly Ru free.
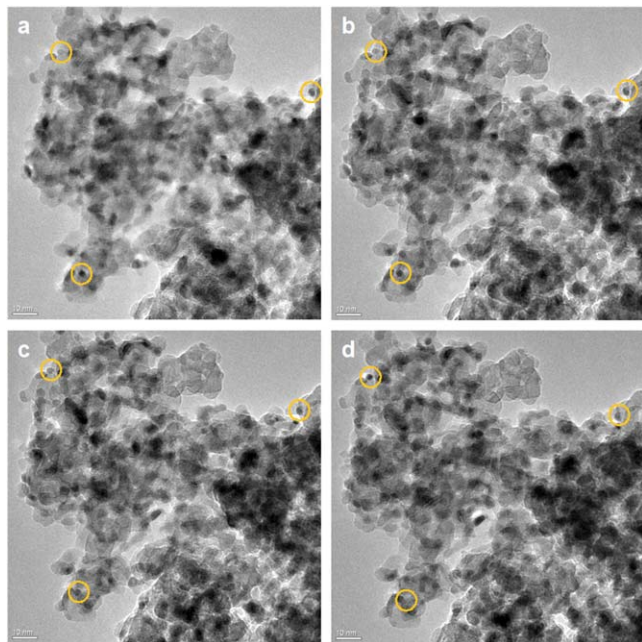
Figure A·2. Example of the use of individual images from the high resolution tomographic TEM series of Ru/TiO$_x$/C$^{400°C,H_2}$ (see file HR_RuTiOxC-400_TOMO.avi in the SI) for the determination of the Ru particle size, whereby the angle of the sample holder was varied by 2° for each frame from (a) to (d). Exemplarily, the circles indicate the position of three individual Ru particles in each frame, whereby the comparison of the images enables the identification of Ru particles and the assessment of the particle size distribution depicted in Fig. 1h.

ORCID

Björn M. Stühmeier ⓘ https://orcid.org/0000-0001-7713-2261
Robin J. Schuster ⓘ https://orcid.org/0000-0003-4144-8680
Louis Hartmann ⓘ https://orcid.org/0000-0002-3964-1935
Hubert A. Gasteiger ⓘ https://orcid.org/0000-0001-8199-8703

References

1. S. van Renssen, *Nat. Clim. Change*, **10**, 799 (2020).
2. M. Noussan, P. P. Raimondi, R. Scita, and M. Hafner, *Sustainability*, **13**, 298 (2021).
3. M. M. Whiston, I. L. Azevedo, S. Litster, K. S. Whitefoot, C. Samaras, and J. F. Whitacre, *Proc. Natl. Acad. Sci. USA*, **116**, 4899 (2019).
4. A. T. Mayyas, M. F. Ruth, B. S. Pivovar, G. Bender, and K. B. Wipke, *Manufacturing cost analysis for proton exchange membrane water electrolyzers NREL/TP-6A20-72740*, National Renewable Energy Lab. (NREL), Golden, CO (United States) (2019).
5. L. Du, V. Prabhakaran, X. Xie, S. Park, Y. Wang, and Y. Shao, *Adv. Mater.*, **33**, 1908232 (2021).
6. R. L. Borup, A. Kusoglu, K. C. Neyerlin, R. Mukundan, R. K. Ahluwalia, D. A. Cullen, K. L. More, A. Z. Weber, and D. J. Myers, *Curr. Opin. Electrochem.*, **21**, 192 (2020).
7. M. Bernt, A. Hartig-Weiß, M. F. Tovini, H. A. El-Sayed, C. Schramm, J. Schröter, C. Gebauer, and H. A. Gasteiger, *Chem. Ing. Tech.*, **92**, 31 (2020).
8. M. Bernt, A. Siebel, and H. A. Gasteiger, *J. Electrochem. Soc.*, **165**, F305 (2018).
9. H. A. Gasteiger, J. E. Panels, and S. G. Yan, *J. Power Sources*, **127**, 162 (2004).
10. K. Ayers, N. Danilovic, R. Ouimet, M. Carmo, B. Pivovar, and M. Bornstein, *Annu. Rev. Chem. Biomol. Eng.*, **10**, 219 (2019).
11. 'Fuel Cell Technologies Program Multi-Year Research, Development, and Demonstration Plan', U.S. Department of Energy (2005, revision: 2012, accessed: 11/12/2021) (https://energy.gov/eere/fuelcells/downloads/hydrogen-and-fuel-cell-technologies-office-multi-year-research-development).
12. A. Kongkanand and M. F. Mathias, *J. Phys. Chem. Lett.*, **7**, 1127 (2016).
13. J. N. Schwämmlein, P. J. Rheinländer, Y. Chen, K. T. Freyer, and H. A. Gasteiger, *J. Electrochem. Soc.*, **165**, F1312 (2018).
14. W. R. Baumgartner, P. Parz, S. D. Fraser, E. Wallnöfer, and V. Hacker, *J. Power Sources*, **182**, 413 (2008).
15. C. A. Reiser, L. Bregoli, T. W. Patterson, J. S. Yi, J. D. Yang, M. L. Perry, and T. D. Jarvi, *Electrochem. Solid-State Lett.*, **8**, A273 (2005).
16. G. S. Harzer, J. N. Schwämmlein, A. M. Damjanović, S. Ghosh, and H. A. Gasteiger, *J. Electrochem. Soc.*, **165**, F3118 (2018).
17. S. Trasatti, *J. Electroanal. Chem. Interf. Electrochem.*, **111**, 125 (1980).
18. Y. Lee, J. Suntivich, K. J. May, E. E. Perry, and Y. Shao-Horn, *J. Phys. Chem. Lett.*, **3**, 399 (2012).
19. S. D. Knights, K. M. Colbow, J. St-Pierre, and D. P. Wilkinson, *J. Power Sources*, **127**, 127 (2004).
20. N. A. Anastasijević, Z. M. Dimitrijević, and R. R. Adžić, *Electrochim. Acta,*, **31**, 1125 (1986).
21. J. Durst, A. Orfanidi, P. J. Rheinländer, F. Hasché, C. Eickes, P. Suchsland, M. Binder, and H. A. Gasteiger, *ECS Trans.*, **69**, 67 (2015).
22. C. Bracchini, V. Indovina, S. D. Rossi, and L. Giorgi, *Catal. Today*, **55**, 45 (2000).
23. H. A. Gasteiger, N. M. Markovic, and P. N. Ross, *J. Phys. Chem.*, **99**, 8290 (1995).
24. M. S. Rau, M. R. Gennero de Chialvo, and A. C. Chialvo, *Electrochim. Acta,*, **55**, 5014 (2010).
25. B. M. Stühmeier, M. R. Pietsch, J. N. Schwämmlein, and H. A. Gasteiger, *J. Electrochem. Soc.*, **168**, 064516 (2021).
26. G. L. Haller and D. E. Resasco, *Advances in Catalysis*, ed. D. D. Eley et al. (Academic, New York, NY) 36, p. 173 (1989).
27. S. Tauster, *Acc. Chem. Res.*, **20**, 389 (1987).
28. J. Zhang, M. Zhang, Z. Jin, J. Wang, and Z. Zhang, *Appl. Surf. Sci.*, **258**, 3991 (2012).
29. A. D. Logan, E. J. Braunschweig, A. K. Datye, and D. J. Smith, *Langmuir*, **4**, 827 (1988).
30. Q. Fu and T. Wagner, *Surf. Sci. Rep.*, **62**, 431 (2007).
31. C.-J. Pan, M.-C. Tsai, W.-N. Su, J. Rick, N. G. Akalework, A. K. Agegnehu, S.-Y. Cheng, and B.-J. Hwang, *J. Taiwan Inst. Chem. Eng.*, **74**, 154 (2017).
32. D. Banham, S. Ye, A. O'Toole, A. Lemke, and E. Eisenbraun, *Nano Energy*, **27**, 157 (2016).
33. V. Viswanathan, K. L. Pickrahn, A. C. Luntz, S. F. Bent, and J. K. Nørskov, *Nano Lett.*, **14**, 5853 (2014).
34. T. N. Geppert, M. Bosund, M. Putkonen, B. M. Stühmeier, A. T. Pasanen, P. Heikkilä, H. A. Gasteiger, and H. A. El-Sayed, *J. Electrochem. Soc.*, **167**, 084517 (2020).
35. B. M. Stühmeier, S. Selve, M. U. M. Patel, T. N. Geppert, H. A. Gasteiger, and H. A. El-Sayed, *ACS Appl. Energy Mater.*, **2**, 5534 (2019).
36. H. Shintani, Y. Kojima, K. Kakinuma, M. Watanabe, and M. Uchida, *J. Power Sources*, **294**, 292 (2015).
37. E. Hornberger et al., *ACS Catal.*, **8**, 9675 (2018).
38. B.-J. Hsieh, M.-C. Tsai, C.-J. Pan, W.-N. Su, J. Rick, H.-L. Chou, J.-F. Lee, and B.-J. Hwang, *Electrochim. Acta*, **224**, 452 (2017).
39. Y. Zhou, Z. Xie, J. Jiang, J. Wang, X. Song, Q. He, W. Ding, and Z. Wei, *Nat. Catal.*, **3**, 454 (2020).
40. T. Suoranta, M. Niemelä, and P. Perämäki, *Talanta*, **119**, 425 (2014).
41. T. Mittermeier, P. Madkikar, X. Wang, H. A. Gasteiger, and M. Piana, *J. Electrochem. Soc.*, **163**, F1543 (2016).
42. J. N. Schwämmlein, B. M. Stühmeier, K. Wagenbauer, H. Dietz, V. Tileli, H. A. Gasteiger, and H. A. El-Sayed, *J. Electrochem. Soc.*, **165**, H229 (2018).
43. P. J. Rheinländer, J. Herranz, J. Durst, and H. A. Gasteiger, *J. Electrochem. Soc.*, **161**, F1448 (2014).
44. H. A. Gasteiger, W. Gu, R. Makharia, M. F. Mathias, and B. Sompalli, "Handbook of fuel cells—fundamentals, technology and applications.", ed. W. Vielstich, H. A. Gasteiger, and A. Lamm *Fuel Cell Technology and Applications* (Wiley, Hoboken, New York) 3, p. 593 (2003).
45. T. Mittermeier, A. Weiß, H. A. Gasteiger, and F. Hasché, *J. Electrochem. Soc.*, **164**, F1081 (2017).
46. D. J. Morgan, *Surf. Interface Anal.*, **47**, 1072 (2015).
47. A. Fujimoto, Y. Yamada, M. Koinuma, and S. Sato, *Anal. Chem.*, **88**, 6110 (2016).
48. C. Simon, F. Hasché, D. Müller, and H. A. Gasteiger, *ECS Trans.*, **69**, 1293 (2015).
49. C. Simon, F. Hasché, and H. A. Gasteiger, *J. Electrochem. Soc.*, **164**, F591 (2017).
50. S. Bernal, J. J. Calvino, M. A. Cauqui, J. M. Gatica, C. L. Cartes, J. A. P. Omil, and J. M. Pintado, *Catal. Today*, **77**, 385 (2003).
51. S. Tauster, S. Fung, and R. L. Garten, *J. Am. Chem. Soc.*, **100**, 170 (1978).
52. H. A. Gasteiger, N. Markovic, P. N. Ross, and E. J. Cairns, *J. Phys. Chem.*, **97**, 12020 (1993).
53. Y. Sugawara, A. P. Yadav, A. Nishikata, and T. Tsuru, *J. Electrochem. Soc.*, **155**, B897 (2008).
54. R. Prins, *Chem. Rev.*, **112**, 2714 (2012).
55. W. Karim, C. Spreafico, A. Kleibert, J. Gobrecht, J. VandeVondele, Y. Ekinci, and J. A. van Bokhoven, *Nature*, **541**, 68 (2017).
56. M. P. Seah and W. A. Dench, *Surf. Interface Anal.*, **1**, 2 (1979).
57. J. Durst, C. Simon, F. Hasché, and H. A. Gasteiger, *J. Electrochem. Soc.*, **162**, F190 (2015).
58. J. Zheng, Y. Yan, and B. Xu, *J. Electrochem. Soc.*, **162**, F1470 (2015).
59. L. Gancs, B. N. Hult, N. Hakim, and S. Mukerjee, *Electrochem. Solid-State Lett.*, **10**, B150 (2007).
60. P. Piela, C. Eickes, E. Brosha, F. Garzon, and P. Zelenay, *J. Electrochem. Soc.*, **151**, A2053 (2004).
61. S. Martens et al., *J. Power Sources*, **392**, 274 (2018).
62. A. Kusoglu, D. Kushner, D. K. Paul, K. Karan, M. A. Hickner, and A. Z. Weber, *Adv. Funct. Mater.*, **24**, 4763 (2014).
63. M. A. Modestino, A. Kusoglu, A. Hexemer, A. Z. Weber, and R. A. Segalman, *Macromolecules*, **45**, 4681 (2012).

64. C. Jackson, G. T. Smith, M. Markiewicz, D. W. Inwood, A. S. Leach, P. S. Whalley, A. R. Kucernak, A. E. Russell, D. Kramer, and P. B. J. Levecque, *J. Electroanal. Chem.*, **819**, 163 (2018).
65. M. Wesselmark, B. Wickman, C. Lagergren, and G. Lindbergh, *Electrochem. Commun.*, **12**, 1585 (2010).
66. C. M. Zalitis, J. Sharman, E. Wright, and A. R. Kucernak, *Electrochim. Acta*, **176**, 763 (2015).
67. H.-Y. Lin and Y.-W. Chen, *Thermochim. Acta*, **419**, 283 (2004).
68. W. Vogel, L. Lundquist, P. Ross, and P. Stonehart, *Electrochim. Acta*, **20**, 79 (1975).
69. K. Lu, Y. J. Kuo, and B. J. Tatarchuk, *J. Catal.*, **116**, 373 (1989).
70. M. J. Muñoz-Portero, J. García-Antón, J. L. Guiñón, and R. Leiva-García, *Corros. Sci.*, **53**, 1440 (2011).
71. M. Sulek, J. Adams, S. Kaberline, M. Ricketts, and J. R. Waldecker, *J. Power Sources*, **196**, 8967 (2011).
72. T. A. Greszler, T. E. Moylan, and H. A. Gasteiger, "Handbook of fuel cells—fundamentals, technology and applications." ed. W. Vielstich, H. Yokokawa, and H. A. Gasteiger *Advances in Electrocatalysis, Materials, Diagnostics and Durability* (Wiley, Hoboken) 6, p. 729 (2009).
73. J. Zhang, F. Coms, and S. Kumaraguru, *J. Electrochem. Soc.*, **168**, 024520 (2021).
74. H. Tian, X. Cui, and J. Shi, *Chem. Eng. J.*, **421**, 129430 (2021).
75. A. Lewera, L. Timperman, A. Roguska, and N. Alonso-Vante, *J. Phys. Chem. C*, **115**, 20153 (2011).
76. J. S. Newman, *Electrochemical Systems* (Prentice Hall, Englewood Cliffs) (1991).
77. J. Zheng, J. Nash, B. Xu, and Y. Yan, *J. Electrochem. Soc.*, **165**, H27 (2018).
78. J. Zheng, W. Sheng, Z. Zhuang, B. Xu, and Y. Yan, *Sci. Adv.*, **2**, e1501602 (2016).
79. J. Durst, A. Siebel, C. Simon, F. Hasche, J. Herranz, and H. A. Gasteiger, *Energy Environ. Sci.*, **7**, 2255 (2014).